UNIVERSIDADE DE SÃO PAULO
Instituto de Física de São Carlos

Proceedings of the seminar to the course

Chemical Physics and Thermodynamics of Gases and Solids

SFI5769 / 2025-1

Ph.W. Courteille (editor)
Universidade de São Paulo
Instituto de Física de São Carlos
30/06/2025

.

Contents

Preface

Estes anais (ou proceedings) reúnem as monografias elaboradas pelos alunos do curso de Fundamentos da Interação da Radiação com a Matéria (SFI5905), realizado no Instituto de Física de São Carlos da Universidade de São Paulo durante o primeiro semestre de 2023 sob supervisão do Prof. Ph. W. Courteille.

1

The Ising model

Claudio Alves Pessoa Junior

Instituto de Física de São Carlos, Universidade de São Paulo, 13560-970 São Carlos, SP, Brazil

Abstract: The Lenz-Ising model serves as a foundational framework for studying phase transitions in statistical mechanics. This work explores the analytical solution for a 2D square lattice, focusing on critical temperature and thermodynamic properties such as energy, magnetization, heat capacity, and susceptibility. Using Monte-Carlo simulations and the Metropolis algorithm, we numerically validate Onsager's exact results, demonstrating a critical exponent $\gamma = (1.737 \pm 0.014)$, closely matching the theoretical value of 7/4. The study highlights the model's utility in computational physics and its role in verifying numerical methods for complex systems.

1.1 A brief history

In 1924, Ernst Ising solved the one-dimensional case of this model in his thesis [1] following a suggestion from his advisor, Wilhelm Lenz. Now known as the Lenz-Ising Model (or simply Ising Model), it has proven to be a powerful mathematical framework for describing interactions between discrete variables, such as spin-spin interactions. The model employs statistical physics to derive useful properties of lattices composed of magnetic dipole moments (or atomic spins). In his thesis, Ising studied the dynamics of phase transitions in a 1D lattice, ultimately discovering the absence of a phase transition. This finding led him to pursue a career in teaching at a university, setting aside further research until after World War II.

"When Hitler came to power in 1933 I was dismissed from public schools, and for four years I was the head of a private Jewish school near Potsdam. I left Germany in 1939, but was not able to come to the U.S.A. immediately. Only after I had come to this country USA in 1947 did I learn that the idea had been expanded. I have tried to extend my model to more complicated forms, but have not published anything yet.", Ising wrote [2].

In 1947, Lars Onsager analytically solved the two-dimensional square-lattice case [3], one of the simplest nontrivial systems in statistical mechanics where phase transitions can be observed—a topic we will explore in this proceeding [4]. Notably, microscopic short-range interactions in this model can produce phase transitions that differ fundamentally in character from classical van der Waals (or Curie-Weiss/mean-field) transitions.

1.2 Theoretical description

Since no phase transition occurs in one dimension, we will explore the fundamentals of the simplest case where phase transitions are possible: a two-dimensional square spin lattice. First, we consider that each particle can be in one of two states: spin up (+1) or spin down (−1). The spin of the k-th particle is indicated by $\sigma_k \in \{-1, +1\}$, where $k \in \{1, \ldots, L^d\}$, with L being the linear size of the lattice (number of particles along each dimension) and $d = 2$ the spatial dimension. The spin configuration of the entire lattice is represented by $\boldsymbol{\sigma} = (\sigma_1, \ldots, \sigma_k, \ldots, \sigma_{L^2})$. There are 2^N possible spin configurations $\boldsymbol{\sigma}$, where $N = L^2$ is the total number of particles. A visualization of this lattice is shown in Figure 1.1.

This model assumes that the energy includes interaction terms between neighboring spins. When an external magnetic field is present, the system has no analytical solution in general. The Hamiltonian describing the energy is given by

$$E(\boldsymbol{\sigma}) = -J_{ij} \sum_{\langle ij \rangle}^{N} \sigma_i \sigma_j - B \sum_{i}^{N} \sigma_i, \tag{1.1}$$

where J_{ij} represents the coupling constant between

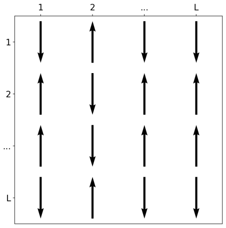

Figure 1.1: Representation of a square lattice of spins.

spins σ_i and σ_j, and B denotes the strength of the external magnetic field. Spin-spin interactions can be classified into three types:

- Ferromagnetic ($J_{ij} > 0$)
- Antiferromagnetic ($J_{ij} < 0$)
- Non-interacting ($J_{ij} = 0$).

To simplify our system, we assume uniform nearest-neighbor interactions, setting $J_{ij} \equiv J$ for all adjacent spins. Furthermore, considering the case without an external magnetic field ($B = 0$) and generalizing to a two-dimensional lattice, we can express the energy as

$$E(\boldsymbol{\sigma}) = -J \sum_{i=1}^{L} \sum_{j=1}^{L-1} \sigma_{i,j}\sigma_{i,j+1} - J \sum_{i=1}^{L-1} \sum_{j=1}^{L} \sigma_{i,j}\sigma_{i+1,j}. \tag{1.2}$$

We can now establish the general partition function within the grand canonical ensemble formalism [5]

$$Z_\Lambda(T) \equiv Z_\Lambda = \sum_{\sigma \in \Lambda} e^{-\beta E(\sigma)}, \tag{1.3}$$

where Λ represents the set of all possible spin configurations $\boldsymbol{\sigma}$, and $\beta = \frac{1}{k_B T}$ is the inverse temperature (with k_B denoting the Boltzmann constant and T the absolute temperature).

Substituting the expression of energy from Equation 1.2 into the partition function Equation 1.3, and utilizing two key observations

- The identity $(\sigma_{ij}\sigma_{lm})^2 \equiv 1$ for spins $\sigma \in \{-1, +1\}$
- The hyperbolic trigonometric identity $e^{\beta J \sigma_{ij}\sigma_{lm}} = \cosh(\beta J) + \sigma_{ij}\sigma_{lm}\sinh(\beta J)$

we can develop a geometric interpretation of the partition function in terms of polygon configurations. The expansion of the product of all nearest-neighbor terms in the partition function naturally leads to a description where

- Each term in the expansion corresponds to a collection of closed polygons (or "contours") on the dual lattice
- These polygons represent domain boundaries between regions of aligned spins
- The weight of each configuration depends on the total length of these boundaries

This polygon representation, illustrated in Figure 1.2, provides a powerful geometric framework for analyzing the Ising model, where

$$Z_\Lambda = (2\cosh^2 \beta J)^N \sum_{\text{polygons}} (\tanh \beta J)^{\text{total perimeter}} \tag{1.4}$$

with $N = L^2$ being the number of lattice sites. The summation runs over all possible closed polygon configurations on the lattice.

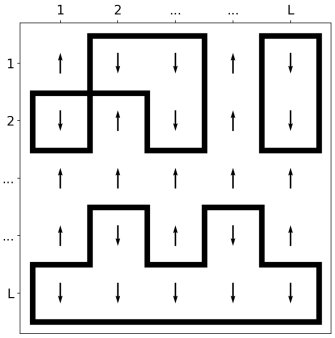

Figure 1.2: Example of polygons in a spin-state σ. Here $P_4(\sigma) = 1$, $P_6(\sigma) = 1$, $P_8(\sigma) = 1$, $P_{16}(\sigma) = 1$ and $P_n(\sigma) = 0$ if $n \notin \{4, 6, 8, 16\}$. It is possible to see that all n are always even and $n \in [4, 2(N - L)]$.

From Equation 1.4, we can work on $\sum_{\text{polygons}}$ in order to obtain the partition function for a finite lattice

$$Z_\Lambda = (\cosh \beta J)^{2(N-L)}\, 2^N \sum_{n \geq 0} P_n(\sigma)\, (\tanh \beta J)^n\,, \tag{1.5}$$

where n is the perimeter length of a polygon and $P_n(\sigma)$ the number of closed polygons with perimeter n for a given spin configuration $\sigma \in \Lambda$, always depending on the lattice topology and boundary conditions.

In this work, we focus on key physical quantities of the Ising system. Having established the energy formulation, we now examine the magnetization M, which quantifies the net alignment of spins as magnetic dipoles. The total magnetization is defined as the sum over all spin states

$$M(\boldsymbol{\sigma}) = \sum_{i=1}^{N} \sigma_i, \tag{1.6}$$

where $N = L^2$ is the total number of spins. This quantity serves as an order parameter for the ferromagnetic phase transition. In the ordered phase at low temperatures, the spins align preferentially, which makes the magnetization scale $|M| \sim \mathcal{O}(N)$. In the disordered high-temperature phase, random spin configurations cause the magnetization to fluctuate around zero with typical values of order $\mathcal{O}(\sqrt{N})$, while the expectation value $\langle M \rangle$ vanishes due to symmetry. The temperature dependence of $\langle |M| \rangle$ reveals the spontaneous symmetry breaking at the critical temperature T_c, where the system transitions between these two regimes.

We now derive the material properties related to energy and magnetization. Following standard statistical mechanics, the heat capacity C_V and magnetic susceptibility χ are defined through the temperature and field derivatives of the ensemble averages

$$C_V = \frac{\partial \langle E \rangle}{\partial T}, \quad \chi = \frac{\partial \langle M \rangle}{\partial B}, \tag{1.7}$$

these can be expressed more operationally in terms of fluctuations as

$$\begin{aligned} C_V &= \frac{\langle E^2 \rangle - \langle E \rangle^2}{k_B T^2}, \\ \chi &= \frac{\langle M^2 \rangle - \langle M \rangle^2}{k_B T}, \end{aligned} \tag{1.8}$$

where the angle brackets denote thermal averages. Our analysis will utilize all four fundamental quantities: the energy Equation 1.2, magnetization Equation 1.6, and these material properties Equation 1.8, which connect microscopic configurations to macroscopic observables. The heat capacity characterizes energy fluctuations, while the susceptibility quantifies how the magnetization responds to external fields, both revealing critical behavior near phase transitions.

1.2.1 Phase transitions

In general, phase transitions can be identified by examining the analytic properties of the system's thermodynamic functions. However, for the Ising model, it is more practical to detect these transitions through macroscopic instabilities, particularly through characteristic changes in the temperature dependence of thermodynamic quantities. The critical temperature T_c emerges as a key parameter where derivatives of macroscopic variables (such as magnetization or specific heat) exhibit singular behavior, signaling the onset of long-range order.

Critical temperature

For anisotropic couplings where J is different in each direction (horizontal and vertical), $J_H \neq J_V$, we define $K = J_H/(k_B T)$, $L = J_V/(k_B T)$ and apply the Kramers-Wannier duality [6]. The partition function exhibits dual forms

$$\begin{aligned} \text{Low } T: Z_N &= 2e^{N(\tilde{K}+\tilde{L})} \sum_{\tilde{P}} e^{-2(\tilde{K}h+\tilde{L}v)} \\ \text{High } T: Z_N &= 2^N (\cosh K \cosh L)^N \\ &\quad \times \sum_{P} (\tanh L)^v (\tanh K)^h \end{aligned}$$

where $\tilde{K}, \tilde{L}$ are dual couplings ($\tanh \tilde{K} = e^{-2L}$), P ($\tilde{P}$) are original (dual) polygons, and h, v count horizontal/vertical bonds. This reveals the temperature duality of the anisotropic model [7].

For a square lattice with isotropic couplings ($J_H = J_V \equiv J$), the critical point occurs when $K = \tilde{K}$. This yields the condition

$$\sinh\left(\frac{2J}{k_B T_C}\right) = 1, \tag{1.9}$$

which can be solved analytically using the identity $\sinh^{-1}(1) = \ln(1+\sqrt{2})$. The exact critical temperature is

$$\frac{k_B T_C}{J} = \frac{2}{\ln(1+\sqrt{2})} \approx 2.26918531421. \tag{1.10}$$

This celebrated result matches Onsager's exact solution for the 2D Ising model.

Critical exponents and thermodynamical variables

The existence of a critical temperature T_C (Equation 1.10) allows us to characterize the phase transition through the magnetization M. This quantity serves as an order parameter, clearly distinguishing between

- The high-temperature paramagnetic phase ($T > T_C$), where spins are randomly oriented and $\langle M \rangle = 0$;

- The low-temperature ferromagnetic phase ($T < T_C$), where spins align spontaneously and $\langle M \rangle \neq 0$.

The transition manifests most dramatically in the magnetic susceptibility χ, which diverges at $T = T_C$ due to the onset of long-range order. This critical behavior reflects the system's sensitivity to infinitesimal perturbations near the phase transition.

Near the critical temperature T_C, thermodynamic quantities exhibit power-law behavior characterized by critical exponents. The heat capacity and magnetic susceptibility scale as

$$\begin{aligned} C_V(T \to T_C^-) &\sim |T - T_C|^{-\alpha} \\ \chi(T \to T_C^-) &\sim |T - T_C|^{-\gamma}, \end{aligned} \tag{1.11}$$

with known Onsager solution values $\alpha = 0$ (logarithmic divergence) and $\gamma = 7/4$ for the 2D Ising model. The zero exponent α indicates a logarithmic rather than algebraic divergence in C_V, while γ governs the susceptibility's singular behavior.

As we define a region where $T \sim T_C$, we must introduce the correlation length. Near the critical temperature, the correlation increases and spin interactions become stronger, so the correlation length reflects both temperature and material properties

$$\xi \approx (T_C - T)^{-\nu}. \tag{1.12}$$

In a second-order phase transition, the correlation length diverges and spans the entire system. However, since we are limited by the lattice size L, we consider

$$\xi \approx L \approx (T_C - T)^{-\nu} \tag{1.13}$$

relating this to the scaling of physical quantities, we obtain

$$\begin{aligned} C_V &\approx L^{-\alpha/\nu} \\ \chi &\approx L^{-\gamma/\nu} \end{aligned} \tag{1.14}$$

thus, values for α and γ can be extracted by analyzing these material properties.

To observe these effects, we perform numerical simulations on lattices of different sizes, as presented below.

1.3 Numerical solution of a 2D squared lattice

Now, based on the considerations of our analytical 2D square lattice and using $C{+}{+}$, we can develop a numerical solution. There are several methods to address this problem [8]; here, we will use a Monte Carlo simulation combined with the Metropolis algorithm.

1.3.1 Monte-Carlo simulation

This technique was developed by mathematicians and first applied in physics during nuclear weapons research [9]. The idea is based on a statistical principle that can be illustrated with a simple example

- **(i)** consider a circle inscribed in a square;
- **(ii)** we know that the ratio of the area of the circle to the area of the square is $\pi/4$;
- **(iii)** if we randomly choose a point within the square, there is a probability of $\pi/4$ that the point also lies inside the circle;
- **(iv)** by generating a large number of random points inside the square and counting how many fall within the circle, we can estimate this probability.

The more points we generate, the closer the estimated value gets to the actual value of $\pi/4$.

1.3.2 Metropolis algorithm

The Metropolis algorithm is a statistical method based on Monte Carlo sampling. It was developed by Metropolis [10], later generalized by Hastings [11], and widely applied in physics. The central idea is to evaluate the "variation" of the partition function by considering the energy difference between two states that differ by a single spin flip.

We calculate ΔE. If $\Delta E \leq 0$, the spin flip is accepted. Otherwise, we compute $z = e^{-\beta \Delta E}$ and generate a random number $r \in [0, 1]$. If $r \leq z$, the new spin configuration is accepted; if not, we reject the change and return to the previous state before proceeding to the next step.

1.3.3 Results

As previously said, the 2D Lenz-Ising model is a great way to check the correctness of a complicated simulation. In order to do a didatic help, in here we present this test. All simulations shown here was inspired by HJORTH-JENSEN [12].

We initialize a 2D lattice with all spins up and evolve it using a Monte Carlo simulation to evaluate the final distribution of spins through the mean values of E, M, C_V, and χ. This evolution is carried out using the Metropolis algorithm, where only a single spin is flipped at each step. Simulations were performed for 12 lattice sizes, with $L \in \{10, 15, 20, 25, 30, 40, 50, 60, 70$

Calculating sums such as E and M directly is computationally expensive and inefficient for numerical simulations. One way to improve efficiency is to compute the energy difference ΔE resulting from a single spin flip (up to down or down to up), and use the Metropolis algorithm to decide whether to accept the change. If the change is accepted, ΔE is added to the initial energy, which is given by $E_{\text{ini}} = -2N$. Magnetization is updated similarly, starting from $M_{\text{ini}} = N$.

With the energy and magnetization computed, the quantities in Equation 1.8 can be evaluated. The results for these four variables are shown in Figure 1.3, Figure 1.4, Figure 1.5, and Figure 1.6. **Note:** All simulations were performed using $k_B = J = 1$ to reduce computational complexity and processing time.

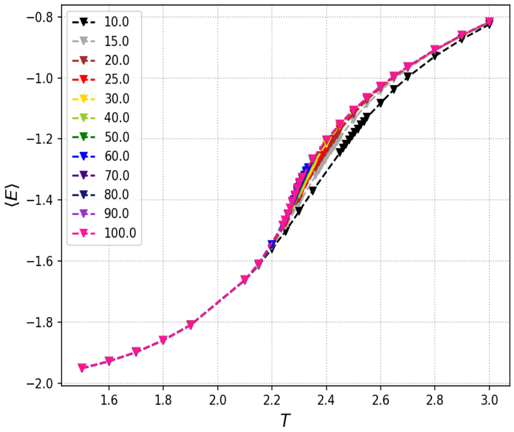

Figure 1.3: Mean energy per particle for different lattices.

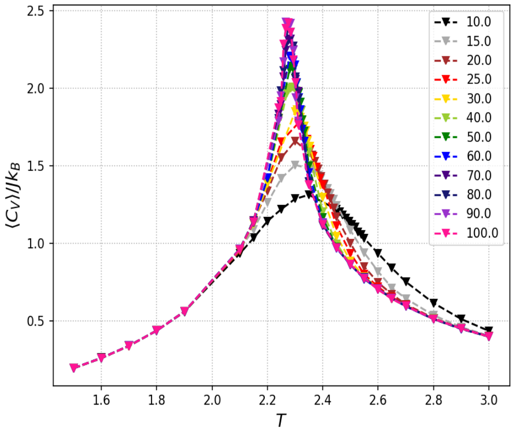

Figure 1.4: Mean heat capacity per particle for different lattices.

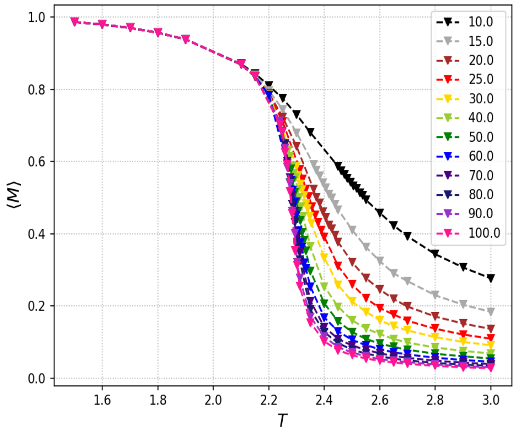

Figure 1.5: Mean magnetization per particle for different lattices.

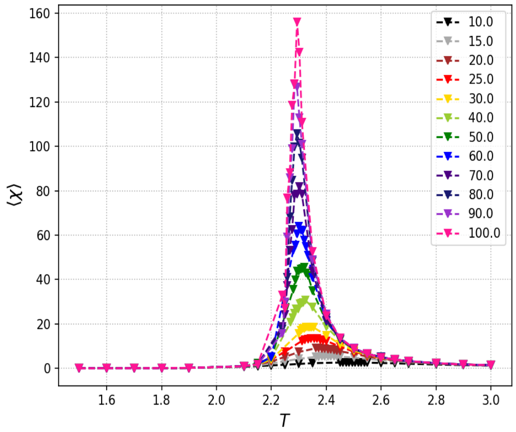

Figure 1.6: Mean magnetic susceptibility per particle for different lattices.

Using 10^6 Monte Carlo steps per lattice size L, we locate $T_C^{(N)}$ at the peak of $\langle \chi \rangle$. The finite-size scaling behavior follows

$$\left| \frac{T_C^{(N)} - T_C}{T_C} \right| = L^{-1/\nu}, \tag{1.15}$$

where T_C is the exact value from Equation 1.10. The maximum susceptibility scales as

$$\chi_{\max} \sim L^{-\gamma/\nu}. \tag{1.16}$$

For the 2D Ising model ($\nu = 1$, $\gamma = 7/4$), this allows direct comparison between our simulated γ and the exact value.

From log-log fits of Equation 1.15 and Equation 1.16 in Figure 1.7, we extract slopes $-1/\nu$ (temperature scaling) and $-\gamma/\nu$ (susceptibility). Our result $\gamma = (1.737 \pm 0.014)$ matches the exact 2D Ising value $\gamma_{\text{exact}} = 7/4 \approx 1.75$.

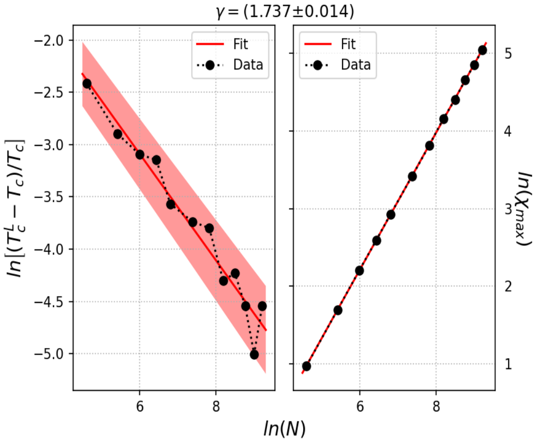

Figure 1.7: Fitting of our simulation, resulting in an error with respect of γ_{real} of -0.7%.

1.4 Conclusion

The 2D Ising model continues to play a vital role in statistical physics, serving as both a fundamental benchmark for numerical methods and a prototype for studying complex systems. In this work, we have presented the complete analytical solution for the square lattice case while simultaneously verifying it through numerical simulations using finite-size scaling techniques.

Our numerical results yield the critical exponent $\gamma = (1.737 \pm 0.014)$, showing remarkable agreement with the theoretical value $\gamma_{\text{exact}} = 7/4 \approx 1.75$ within just 0.7% error. This precision demonstrates how well-designed simulations can effectively approximate thermodynamic limits despite finite-size constraints.

The methodology developed here establishes a solid foundation for investigating more complex spin systems that lack analytical solutions, particularly models with anisotropic interactions, frustrated geometries, or disordered couplings. These extensions are particularly valuable in cases where numerical approaches become the primary tool for understanding emergent phenomena in many-body systems.

Bibliografia

[1] E. Ising. “Contribution to the Theory of Ferromagnetism”, Zeitschrift für Physik, **31**, p. 253-258 (1925).

[2] S. G. Brush. “History of the Lenz-Ising Model”, Reviews of Modern Physics, **39**, p. 883, (1967).

[3] L. Onsager. “A Two-Dimensional Model with and Order-Disorder Transition”, Physical Review, **65**, p. 117, (1944).

[4] G. Gallavotti. “Statistical Mechanics, A Short Treatise”, Springer Berlin Heidelberg, (1999).

[5] P. W. Courteille. “Thermodynamics and Statistical Physics for Material Sciences and Qunatum Gases”, Instituto de Física de São Carlos, (2025).

[6] H. A. Kramers and G. H. Wannier. “Statistical of the Two-Dimensional Ferromagnetic Part I and Part II”, Physical Review, **60**, p. 252-276, (1941).

[7] L. A. Aviles and R. P. Gammag. “Critical temperature in 2D square Ising Model with anisotropic coupling constant using Kramers-Wannier duality”, Journal of Physics: Conference Series, **2543**, p. 012006, (2023).

[8] A. Mainou, N. G. Fytas and M. Weigel. “Efficient algorithms for computing ground states of the 2D randon-field Ising model”, Journal of Physics: Conference Series, **2207**, p. 012009, (2022).

[9] M.H. Kalos and P.A. Whitlock. “Monte Carlo Methods”, WILEY-VCH, (2008).

[10] N. Metropolis, A. W. Rosenbluth, M. N. Rosenbluth, A.H. Teller and E. Teller. “Equation of State Calculations by Fast Computing Machines”, The Journal of Chemical Physics, **21(6)**, p. 1087-1092, (1953).

[11] W. K. Hastings. “Monte Carlo Sampling Methods Using Markov Chains and Their Applications”, Biometrika. **57 (1)**, p. 97-109, (1970).

[12] M. Hjorth-Jensen. “Lecture Notes on Computational Physics”, University of Oslo, (2006).

2

Wigner crystals: On the theoretical prediction and first imaging

Louis Adrian Böhm

Instituto de Física de São Carlos, Universidade de São Paulo, 13560-970 São Carlos, SP, Brazil

Abstract: More than 90 years ago, physicist Eugene Wigner predicted that electrons can form a crystal structure when their kinetic energy is lower than the potential energy of their Coulomb interactions [1, 2]. This exotic phase of matter, formed by electrons, is called the Wigner crystal. In 2024, scientists achieved a major breakthrough by imaging a two-dimensional Wigner crystal for the first time, confirming their theoretical predictions [3]. This highlights that Wigner crystals still remain an active research area and many questions are also still not answered [2]. While this work does not present a new theoretical or experimental result, it instead provides an overview of Wigner crystals, specifically in the context of the course "Chemical Physics and Thermodynamics of Gases and Solids" [4].

2.1 Introduction

In 1934, Eugene Wigner analyzed the properties of free electrons in a metal and predicted that under certain conditions electrons can form solid structures, called Wigner crystals [1]. Achieving this state requires the potential energy of the Coulomb interactions between the electrons to be larger than their kinetic energy. When this condition is met, the electrons will localize in a lattice structure to minimize their energy [1]. Such a state is expected to occur at very low electron densities which makes it difficult to realize in practice [2]. In 1979, Charles Grimes and Gregory Adams observed the resonance expected from a Wigner crystal in an electron system for the first time, indicating that Wigner crystals are indeed a real phenomenon [5]. To achieve this, they studied electrons on the surface of charged liquid Helium which naturally has a very low electron density [5]. However, the direct imaging still remained an outstanding challenge for many more years [2]. It was only later discovered that a Wigner crystals can be achieved more easily by applying a strong magnetic fields [2]. This is due to the fact that the magnetic field forces electrons into discrete energy levels, called Landau levels, and thereby reduces their kinetic energy [6, 3]. Following, their potential energy can then dominate, even at higher electron densities making it much easier to achieve Wigner crystallization. Many works used this technique to indirectly observe Wigner crystals and test their properties [2]. However, a direct observation of the Wigner crystal was only achieved in 2024 by a team of researchers led by Y. Tsui and colleagues. So almost 90 years after Wigner's initial prediction, the first direct imaging of a two-dimensional Wigner crystal confirmed his theory [3]. Since Wigner crystals combine aspects of condensed matter physics and quantum mechanics their study is particularly interesting. For example in condensed matter physics scientist expect that further studies will explain certain anomalies found in specific materials, like the anomalous transport of HgCdTe structures [7]. Further, in the field of quantum mechanics it is expected that studying Wigner crystals will help to understand the quantum Hall effect and quantum phase transition [2].

The following report will start with an introduction to the theoretical framework needed to understand Wigner crystallization. Next the conditions under which Wigner crystals are expected to form are discussed in three separate parts. In the first part it is laid out how Eugene Wigner first predicted electron crystallization. This is followed by a discussion of the phase boundary between the fluid and solid phase of electrons. Finally, in the third part of this section a computational method is presented that can predict precise conditions for Wigner crystallization. Based on this theoretical overview the next part of the report discusses how the first direct imaging of a Wigner crystal was achieved. The report is then finalized with a conclusion of the presented topics.

2.2 Theoretical framework

2.2.1 Jellium model

The model that is often used to describe Wigner crystallization is the Jellium model [8]. It aims to simplify the complex electronic interactions in a metal by assuming that the valence electrons move through a uniform charge background called "Jellium". This background field is constructed by averaging the electric charge of all nuclei and core electrons while disregarding their individual positions. With this the Jellium ensures that the system of electrons is always neutral, since the positive background charge cancels out the negative charges of the electrons [8]. The Jellium model is useful for cases where valence electrons are de-localized and do not participate in chemical bonding. Such is the case for specific metals like Na, K, and Cs [8]. One important parameter in the Jellium model is the Wigner-Seitz radius r_s, which describes the average distance between a pair of electrons in a three dimensional system [8]. It can be derived by considering a sphere of radius R with N uniformly distributed valence electrons within it. This sphere can then be divided into N smaller spheres, each containing one electron [8]. The volume of each of these smaller spheres can then be expressed as:

$$V(r_s) = \frac{V(R)}{N} = \frac{1}{n} \tag{2.1}$$

Where $n = N/V(R)$ is the average valence electron density. To derive the Wigner-Seitz radius r_s the dimensionality of the system needs to considered when calculating $V(r_s)$. For the three-dimensional system it is derived as follows [8].

$$V(r_s) = \frac{4}{3}\pi r_s^3 = \frac{1}{n} \Rightarrow r_s = \left(\frac{3}{4\pi n}\right)^{1/3} \tag{2.2}$$

Following this, one can easily show that for a two-dimensional system it is [7]:

$$r_s = \frac{1}{\sqrt{\pi n}} \tag{2.3}$$

For the rest of the report r_s will be defined dimensionless and in terms of the Bohr radius a_B. For the two-dimensional system it is then given as [7]:

$$r_s = \frac{1}{\sqrt{\pi n}} \cdot \frac{1}{a_B} = \frac{1}{a_B\sqrt{\pi n}} \tag{2.4}$$

2.2.2 Landau levels

By introducing a strong magnetic field into the system of electrons a Wigner crystal can be formed more easily [2]. This is due to the fact that the magnetic field forces the electrons into discrete energy levels, called Landau levels [6]. The following will give a brief overview of the Landau levels and how they are derived.

To adjust the derivation to the problems at hand the Landau Levels are derived for an electron that is confined to the x-y-plane, with electric charge e, which is the elemental charge. A static electromagnetic field $B = Be_z$ with unit vector e_z pointing in z-direction, is introduced. The Schrödinger equation can then be written as [6]:

$$-\frac{\hbar^2}{2m}\left(e_x\frac{\partial}{\partial x} + e_y\frac{\partial}{\partial y} + i\frac{e}{\hbar}\hat{\mathbf{A}}\right)^2 \psi = E\psi \tag{2.5}$$

Where E is the energy of the system, m is the mass of the electron, $\hbar$ is the reduced Planck constant and e_x, e_y are unit vectors in the x and y direction, respectively. The parameter $\hat{\mathbf{A}}$ is the vector potential, which for a uniform magnetic field in the z-direction, can be written as $\hat{\mathbf{A}} = Bxe_y$ [6]. When separating the wavefunction $\psi(x, y)$ into its x and y components $\psi(x, y) = \phi(x)\phi(y)$, it can be written for the eigenstate k_y, as [6]:

$$\psi(x, y) = e^{ik_y y}\phi_{k_y}(x) \tag{2.6}$$

Using this generalized wavefunction the Hamiltonian of the system can be written as [6]:

$$\frac{\hbar^2}{2m}\frac{\partial^2}{\partial x^2}\phi_{k_y}(x) + \frac{1}{2}m\omega_c^2(x - x_0)^2\phi_{k_y}(x) = E\phi_{k_y}(x) \tag{2.7}$$

The full derivation of this equation is given in Appendix 2.6. This equation can be recognized as the equation of a harmonic oscillator, where the electron oscillates with the cyclotron frequency $\omega_c = \frac{|eB|}{m}$ around the center $x_0 = -\frac{\hbar k_y}{eB}$ [6]. Therefore, the energy of the system can be written as [6]:

$$E_n = \hbar\omega_c\left(n + \frac{1}{2}\right) \tag{2.8}$$

In conclusion this shows that electrons in a magnetic field are forced into discrete energy levels, called Landau levels. This reduces their spacial degree of freedom since they are forced to oscillate in an area given by the Landau radius $r_L = \sqrt{\frac{\hbar}{|eB|}}$ [6]. Following this equation, the stronger the magnetic field is the smaller this area gets, meaning the electrons get more localized. Introducing a strong magnetic field helps in the formation of the Wigner crystal, since then the Coulomb interactions and the Landau Levels both force the electrons to localize [3].

2.3 Conditions for Wigner crystallization

2.3.1 Energy Considerations

The key idea of Wigner crystallization is, that when the kinetic energy in an electron gas is lower than the potential energy the electrons will become localized in a lattice structure [1]. To evaluate if this is possible the energies of the two-dimensional electron system will be calculated.

The potential energy of the system is derived by the interaction of two electrons at a distance r via a Coulomb potential energy given by $U_C(r) = \frac{e^2}{4\pi\epsilon r}$ [7]. Here ϵ is the permittivity of the medium. Expressing this potential in terms of the Wigner-Seitz radius r_s, it can be written as:

$$U_C(r_s) = \frac{e^2}{4\pi\epsilon r_s a_B} \tag{2.9}$$

The potential energy is therefore proportional to $1/r_s$.

To then calculate the kinetic energy E_{kin} of the electrons, they are treated as an ideal Fermi gas. The kinetic energy is given by the Fermi energy E_F (Section 4.4 [4]):

$$E_{kin} = E_F = \frac{\hbar^2 k_F^2}{2m_e} \tag{2.10}$$

Where m_e is the electron mass and k_F is the Fermi wave vector. The latter can be expressed in terms of the electron density n as $k_F = \sqrt{2\pi n}$ for the two-dimensional system [7]. The electron density n can then be expressed in terms of the Wigner-Seitz radius r_s as $n = \frac{1}{\pi r_s^2 a_B^2}$. Next, the Fermi wave vector is written as a function of the Wigner-Seitz radius $k_F = \frac{\sqrt{2}}{r_s a_B}$. Substituting this into the equation for the kinetic energy, one gets:

$$E_{kin} = \frac{\hbar^2}{m_e r_s^2 a_B^2} \tag{2.11}$$

Summarizing, this means that the potential energy scales as $1/r_s$ and the kinetic energy as $1/r_s^2$ [1]. In a system with large enough r_s, the potential energy can therefore dominate the kinetic energy [7]. This system therefore needs to have a low electron density, for the Wigner crystallization to occur [2].

2.3.2 Phase boundary

Next the phase transition from an electron liquid to a Wigner crystal will be discussed. The discussion is based on the letter [9] which gives a thermodynamic perspective on this transition. The authors assume a system with constant pressure and temperature. In this isobaric-isothermal system the Gibbs free energy G of the system stays the same (see Section 1.2.3.5 [4]) [9]:

$$G_{fluid} = G_{crystal} \tag{2.12}$$

The Gibbs energy is defined as $G = E + PV - TS$ [4], where E is the internal energy, V is the volume and S is the entropy. From this the following relationship can be derived [9]:

$$\Delta G = \Delta E + P\Delta V - T\Delta S = 0 \tag{2.13}$$

$$\Rightarrow \Delta E = T\Delta S - p\Delta V \tag{2.14}$$

For a system where all interactions are due to the coulomb potential, the relationship between the potential and kinetic energy is given by the Coulombic virial theorem [10]. It can be written as [10, 9]:

$$2E_{kin} + U = 3PV \tag{2.15}$$

Where E_{kin} is the kinetic energy and U is the potential energy of the system. For the phase change this is then written as [9]:

$$2\Delta E_{kin} + \Delta U = 3P\Delta V \tag{2.16}$$

$$\Rightarrow P\Delta V = \frac{2}{3}\Delta E_{kin} + \frac{1}{3}\Delta U \tag{2.17}$$

Since the internal energy E is the sum of the kinetic and potential energy, its change during the phase transition can be expressed as $\Delta E = \Delta E_{kin} + \Delta U$. Combining this with the previous equations, the following can be derived [9]:

$$T\Delta S + \Delta E = \frac{2}{3}\Delta E_{kin} + \frac{1}{3}\Delta U \tag{2.18}$$

$$\Rightarrow T\Delta S = \frac{5}{3}\Delta E_{kin} + \frac{4}{3}\Delta U \tag{2.19}$$

For a constant temperature T and pressure P the kinetic energy of the system stays constant during the phase transition. If $T > 0$ the change of entropy ΔS can be expressed as [9]:

$$\Delta S = \frac{4}{3}\frac{\Delta U}{T} \tag{2.20}$$

And for the change of the Volume one gets [9]:

$$\Delta V = \frac{1}{3}\frac{\Delta U}{P} \tag{2.21}$$

With these results and the Clausius-Clapeyron equation (Section 2.1.2 [4]) the following can be derived [9]:

$$\frac{dP}{dT} = \frac{\Delta S}{\Delta V} = \frac{12}{3}\frac{P}{T} = 4\frac{P}{T} \tag{2.22}$$

This equation is then integrated [9]:

$$\Rightarrow dP = 4\frac{P}{T}dT \tag{2.23}$$

$$\Rightarrow \frac{dP}{P} = 4\frac{dT}{T} \tag{2.24}$$

$$\Rightarrow \ln(P) = 4\ln(T) + const. \tag{2.25}$$

$$\Rightarrow P = CT^4 \tag{2.26}$$

Where C is a constant that depends on the system. In summary, this means that for an isobaric-isotherm electron system the pressure must be proportional to the fourth power of the temperature $P \propto T^4$. Reaching the boundary therefore strongly depends on the temperature. This indicates that the Wigner crystallization is best achieved at a low temperature where the influence of the fourth power of the temperature is minimized.

2.3.3 Computational evaluation

To determine more precise conditions for Wigner crystallization, a computational evaluation of the problem is necessary. In the work [11] the authors use a computational method to determine the Wigner-Seitz radius r_s at which Wigner crystallization is expected to occur. They first set up the Hamiltonian as a function of the Wigner-Seitz radius r_s for a 2D system of N electrons [11]. In this work the authors calculate everything in the units of Rydbers per electron given as $1Ry = \frac{me^4}{2\hbar^2}$ [11]. The Hamiltonian is then given as [11]:

$$\hat{H} = \frac{1}{r_s^2}\sum_{0<i}^{N}\nabla_i^2 + \frac{2}{r_s}\sum_{0<i<j}^{N}\frac{1}{|\hat{\mathbf{r}}_i - \hat{\mathbf{r}}_j|} + const. \tag{2.27}$$

Here $\hat{\mathbf{r}}_i$ is the position operator of the i-th electron and ∇_i^2 is the Laplacian operator acting on the i-th electron. The first term describes the kinetic energy of the system, and the second term describes the potential energy of the system due to the Coulomb interaction. The constant term represents the contribution of the neutralizing background which arises from the Jellium model [11]. The authors then use the variational Monte Carlo (VMC) and the fixed-node Green's function Monte Carlos method (FN-GFMC) to find the ground state of the system under different conditions. Due to the brevity of this report, only the less complex VMC method will be discussed here.

The VMC method is a stochastic method that uses random sampling to find the expected value of a function. Let R be one possible configuration of positions for all N electrons in the system. A trial wave function $\Psi_T(R)$ is chosen, which is assumed to have the correct symmetry. Configurations R are then sampled from the probability density function

$$\frac{|\Psi_T(R)|^2}{\int |\Psi_T(R)|^2 dR} \tag{2.28}$$

The sampling is performed with the Metropolis algorithm, which strategically generates a set of random positions for the electrons in the system [12]. Next the energy for all sampled configurations is calculated using the Hamiltonian $\hat{H}$ of the system. It can be shown that the expectation value from all these energies is an upper bound of the exact ground state energy of the system [11]. The choice of the trail wave function determines which system is described. This way the authors could model the electron system for the gas, liquid and for the crystalline phase [11]. Further, the temperature T of the system is set to T = 0 so that the crystal can be modeled as free of any defects [11]. Figure 2.1 shows the predicted dependency on r_s for the ground state energies of each phase. The graphs are obtained by fitting them to the VMC results, which can also be seen in the figure. For $r_s > 37$ the energy of the crystal phase is the lowest and therefore the system is predicted to crystallize to minimize its energy. The authors give a critical value of $r_s \approx 37 \pm 5$ for the Wigner crystallization. Such a high Wigner-Seitz radius is experimentally difficult to achieve, especially considering the fact that the calculation assumes a nonphysical temperature of T = 0 [11, 7].

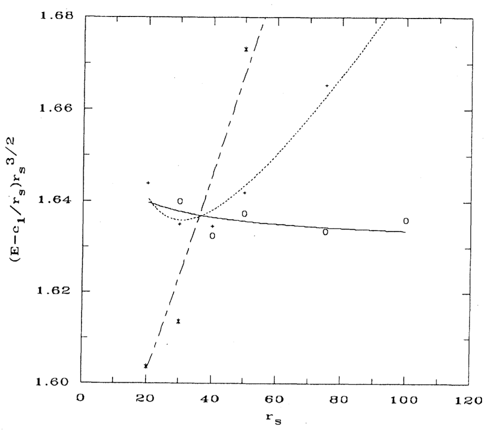

Figure 2.1: The predicted ground state energies of an electron system for different phases as a function of the Wigner-Seitz radius r_s. The electron gas phase is represented by the dashed line, the liquid phase by the dotted and the crystal phase by the solid line. All lines are fitted to the data points given by the MC method: Circles for the crystal, stars for the liquid and plus signs for the gas phase.

2.4 Experimental observations

While an indirect observation of Wigner crystallization has already been done in the past, the first direct imaging of a 2D Wigner crystal was only achieved in 2024, published in paper [3]. The authors use a bilayer graphene sample which forms a 2D electron gas on the surface. The high value for the Wigner-Seitz Radius, which was discussed in the section above would make it hard to achieve Wigner crystallization in such a system. But by applying a strong variable magnetic field, the necessary Wigner-Seitz radius r_s of the system can be tuned [3]. This is due to the Landau levels, which were discussed in section 2.2.2. To image the resulting Wigner crystal the authors used a scanning tunneling microscope (STM) [3].

An STM is a powerful device that can resolve very small scales [3]. This is achieved by moving a sharp conductive tip over the surface of a sample. A voltage is applied between the tip and a sample, which allows electrons to tunnel through the vacuum between them. At a constant bias voltage V_B this tunneling current I depends only on the distance between the tip and the sample. The tip is moved over the whole surface and by measuring this tunneling current, a topographic image of the surface can be created [3]. What makes the imaging approach used in paper [3] novel is that the authors used an ultra-clean bilayer graphene sample to place the Wigner crystal on. This reduces the influence of impurities and defects. The results of the imaging are shown in figure 2.2. In specific, one can see the spatial variation of the tunneling current modulation δI_{dc}, which is the difference between the tunneling current at a specific position and the average tunneling current over the whole surface [3]. While not discussed in this report, the 2D Wigner crystal is expected to show a hexagonal lattice structure [3]. This hexagonal structure is clearly visible in the results of the STM imaging. They further showed that the perturbation of the tunneling current did not destroy the Wigner crystal, which shows that the structure is stable against such disturbances. The results definitively confirm the existence of a Wigner crystals and thereby Wigner's theory [3].

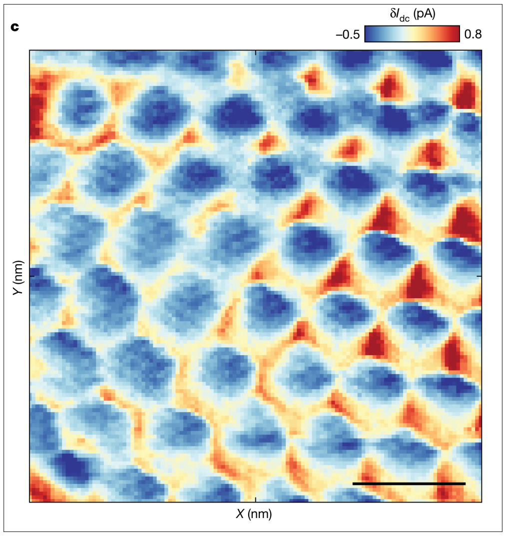

Figure 2.2: Spacial variation of the tunneling current modulation δI_{dc} imaged with an STM. The pattern shows the hexagonal lattice structure of the Wigner crystal. The shown region has a size of 200×200 nm². The scale bar in the bottom right corner corresponds to 50 nm [3].

2.5 Conclusion

In conclusion, this report has discussed the history, the theoretical framework and the first direct imaging of a Wigner crystal. It took 90 years to develop the theoretical and experimental advancements necessary, to achieve this milestone [1, 2]. The report outlines a few of these advancements, like the introduction of the Jellium model, the Landau levels and the computational evaluation of the Wigner-Seitz radius r_s. While this report aims to give an overview of Wigner crystallization, it is by no means exhaustive. The report should rather inspire the reader to further investigate the topic. Especially since many questions are still unanswered, and more theoretical and experimental work will be necessary to fully understand Wigner crystals.

Bibliografia

[1] E. Wigner. On the interaction of electrons in metals. *Physical Review*, 46:1002–1011, 12 1934.

[2] May Chiao. 90 years of the wigner crystal. *Nature Reviews Physics*, 6:348–348, 5 2024.

[3] Yen-Chen Tsui, Minhao He, Yuwen Hu, Ethan Lake, Taige Wang, Kenji Watanabe, Takashi Taniguchi, Michael P. Zaletel, and Ali Yazdani. Direct observation of a magnetic-field-induced wigner crystal. *Nature*, 628:287–292, 4 2024.

[4] Ph.W. Courteille. Thermodynamics and statistical physics.

[5] C. C. Grimes and G. Adams. Evidence for a liquid-to-crystal phase transition in a classical, two-dimensional sheet of electrons. *Physical Review Letters*, 42:795–798, 3 1979.

[6] Kinstantin K. Likharev. 3.2: Landau levels and the quantum hall effect. *Libretexts Physics*, 07, 2025.

[7] *Physics and Chemistry of Low-Dimensional Inorganic Conductors*. Springer US, 1996.

[8] M. Springborg and Y. Dong. *Chapter 4 The Jellium Model*, pages 37–44. Elsevier, 2006.

[9] M Parrinello and N H March. Thermodynamics of wigner crystallization. *Journal of Physics C: Solid State Physics*, 9:L147–L150, 3 1976.

[10] V. B. Bobrov and S. A. Trigger. Virial theorem and gibbs thermodynamic potential for coulomb systems. *Physics of Plasmas*, 21, 10 2014.

[11] B. Tanatar and D. M. Ceperley. Ground state of the two-dimensional electron gas. *Physical Review B*, 39:5005–5016, 3 1989.

[12] Nicholas Metropolis, Arianna W. Rosenbluth, Marshall N. Rosenbluth, Augusta H. Teller, and Edward Teller. Equation of state calculations by fast computing machines. *The Journal of Chemical Physics*, 21:1087–1092, 6 1953.

2.6 Appendix

Derivation of the Landau Level Schrödinger Eq.:

Starting from the Schrödinger Equation 2.5, and using the defined $\hat{\mathbf{A}}$ and generalized eigenfunction:

$$\begin{aligned}-\frac{\hbar^2}{2m}\left(e_x\frac{\partial}{\partial x}+e_y\frac{\partial}{\partial y}+i\frac{e}{\hbar}Bxe_y\right)^2 e^{ik_y y}\phi_{k_y}(x)\\ = Ee^{ik_y y}\phi_{k_y}(x)\end{aligned}$$

Terms in x and y direction have no cross-term:

$$-\frac{\hbar^2}{2m}\left(\frac{\partial^2}{\partial x^2}+\left(\frac{\partial}{\partial y}+i\frac{e}{\hbar}Bxe_y\right)^2\right)e^{ik_y y}\phi_{k_y}(x)$$

Expand second term:

$$-\frac{\hbar^2}{2m}\left(\frac{\partial^2}{\partial x^2}+\frac{\partial^2}{\partial y^2}-\left(\frac{eB}{\hbar}\right)^2+\frac{2ieBx}{\hbar}\frac{\partial}{\partial y}\right)e^{ik_y y}\phi_{k_y}(x)$$

The exponential term of the Eigenfuncion can now be solved:

$$-\frac{\hbar^2}{2m}\left(\frac{\partial^2}{\partial x^2}-k_y^2-\left(\frac{eB}{\hbar}\right)^2-\frac{2k_y eBx}{\hbar}\right)e^{ik_y y}\phi_{k_y}(x)$$

Applying the binomical formula:

$$\left(-\frac{\hbar^2}{2m}\frac{\partial^2}{\partial x^2}+\frac{e^2}{2m}B^2\left(x+\frac{\hbar k_y}{eB}\right)^2\right)e^{ik_y y}\phi_{k_y}(x)$$

With the definition for ω_c and x_0 from the main text, the final equation is obtained.

3

Thermodynamics of mechanochemistry in solid state reactions

Lucas V. C. Militão

Instituto de Física de São Carlos, Universidade de São Paulo, 13560-970 São Carlos, SP, Brazil

Abstract: Mechanochemistry is a promising method for synthesizing advanced materials like co-crystals, which offer the ability to precisely tune critical properties such as drug solubility, stability, and bioavailability. However, the field lacks predictive models that connect machine settings to reaction outcomes, which makes optimizing experiments difficult and often reliant on trial-and-error. This paper aims to solve this by developing a quantitative model based on Hertzian contact theory and Bell's model for reaction kinetics. A direct relationship between milling frequency (f_{mill}) and the resulting contact stress (σ) is derived, showing that stress scales with $f_{\text{mill}}^{2/3}$. The model's most important prediction is a testable hypothesis linking the minimum frequency needed for a reaction ($f_{\text{mill, min}}$) to its activation energy (E_{act}) with the proportionality $f_{\text{mill, min}} \propto E_{\text{act}}^{3/2}$. This provides a path for rationally designing mechanochemical experiments and even selecting for specific products based on their activation energies. While experimental validation is still required, this framework offers a significant step towards a more predictive understanding of mechanochemistry.

3.1 Introduction

3.1.1 Co-crystals

Co-crystals are defined by the IUCr[1] as

> Solid consisting of a crystalline single-phase material composed of two or more different molecular and/or ionic compounds generally in a stoichiometric ratio which are neither solvates nor simple salts.

As such, co-crystals are a class of material that can have a lot of interesting properties for providing a way of changing phasis transition properties without directly changing chemical structure of the given coformers (defined as those molecualar and/or ionic compounds).

Those properties are interesting in the context of biological systems because it is possible to change speed of dissolution, permeability (with supramolecular synthons, that are beyond the scope of this work), and shelf life (if they exist they tend to minimize ΔG).

3.2 Methods

3.2.1 Mechanochemistry

In the search of novel better pathways to chemestry, one of the oldest known synthesys method[2] has shown incredible potential. Mechanochemestry consists on methods that apply physical force to materials instead of heat as a way to promote chemical reactions. There are various ways to do so, ranging from hand-grinding (not very reproducible) to automatic ball mills.

Figure 3.1: Example of equipment used for mechanochemestry, PULVERISETTE 23, obtained from the vendor website

In figure 3.1 it is possible to see an example of a ball mill that is used for mechanochemestry.

3.2.2 Current methods

Some methods are present in the literature to determine activation energies in mechanochemical reactions[2][5], but there is firstly, a lack of information on co-crystalization activation energies, only present on Fischer, *et all*[2] paper. Not only that, but crytical information explaining the correlations between frequency, ball material, equipment geometry, etc is severely missing in the literature. This work also aims to partially solve this problem. One of the works of H. Hergesel [3], demonstrated a significant similarity to some of the proportionality results using the Zhurkov equations. This work improves on it with also showing that it potentially works for crystals. The focus of that work was also on obtaining monomers, so the aims of the works are different.

3.2.3 Bell's model

Mechanichemical kinetics can be described by the Bell's model[6]. In this model, the rate constant without an external force is given by

$$k_0 = A \exp\left(-\frac{E_{\text{act}}}{K_B T}\right) \tag{3.1}$$

Where, E_{act} is defined as the energy encessary to overcome the activation barrier that traps the system in a local energy minima. The reaction rate can therefore be written as

$$k(F) = k_0 \exp\left(\frac{F\Delta\mathbf{x}^{\ddagger}}{k_B T}\right) \tag{3.2}$$

F is defined as a force that modifies the potential by a given activation lenght ($\Delta\mathbf{x}^{\ddagger}$). This in a more usefull format can be written as

$$k(\sigma) = k_0 \exp\left(\frac{\sigma\Delta V^{\ddagger}}{k_B T}\right) \tag{3.3}$$

beign σ defined as the contact stress, or pressure, and the activation volume ($\Delta V^{\ddagger}$), that is the activation lenght multiplied by the area of stress.

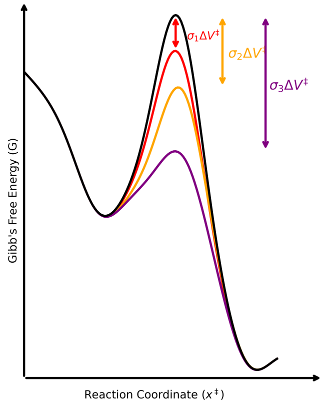

Figure 3.2: Schematic representation of the energy landscape of the reaction. Each curve represents a higher contribution to lowering the activation energy from an external force.

3.3 Results and discussion

3.3.1 Hertzian contact stress

The local stress (σ) during a collision between a milling ball and a crystal particle can be modeled with Hertzian contact theory[3], where an impact force (F_{impact}) is distributed over a small impact radius (R_{impact}).

$$\sigma = \frac{3F_{\text{impact}}}{2\pi R_{\text{impact}}^2} \tag{3.4}$$

The impact force depends on the ball's mass (m) and its maximum acceleration (a_{max}), while the contact area is a function of the ball's radius (r) and the depth of indentation (d).

$$F_{\text{impact}} = ma_{max} \tag{3.5}$$

$$R_{\text{impact}} = (rd)^{\frac{1}{2}} \tag{3.6}$$

From the standard Hertzian force-displacement relationship, where E^* is the reduced Young's modulus, we have:

$$F_{\text{impact}} = \frac{4}{3}E^* r^{\frac{1}{2}} d^{\frac{3}{2}} \tag{3.7}$$

Solving for the indentation depth, d, gives:

$$d = \left(\frac{3}{4}\frac{F_{\text{impact}}}{E^* r^{\frac{1}{2}}}\right)^{\frac{2}{3}} \tag{3.8}$$

Now, it is possible to substitute the expressions for d and F_{impact} back into the primary equation for stress.

$$\sigma = 2\frac{E^* r^{1/2} d^{3/2}}{\pi r d} \tag{3.9}$$

$$= \frac{2}{\pi}E^* r^{-1/2}\left(\frac{3}{4}r^{-1/2}\frac{1}{E^*}F_{\text{impact}}\right)^{1/3} \tag{3.10}$$

$$= \left(\frac{6}{\pi^3}\frac{E^{*2}}{r^2}F_{\text{impact}}\right)^{1/3} \tag{3.11}$$

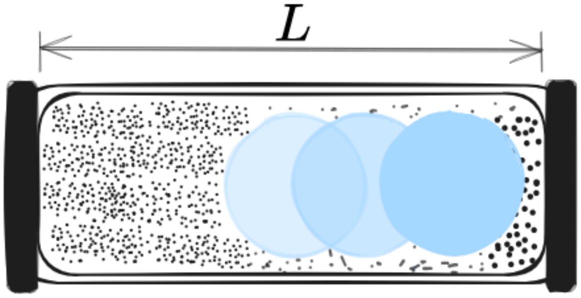

Figure 3.3: Example of ball mill that vibrates in an harmonic like pattern with a constant $\omega_{\text{mill}} = 2\pi f_{\text{mill}}$.

In this model, a sinosoidal movement is assumed in fig. **??**

$$x(t) = x_{\max} \cdot \sin(2\pi f_{\text{mill}} t) \tag{3.12}$$

$$\ddot{x}_{\max} = -x_{\max} \cdot (2\pi f_{\text{mill}})^2 \tag{3.13}$$

$$a_{\max} = |\ddot{x}_{\max}| \tag{3.14}$$

Those parameters are important to relate the theoretical model to the experimental parameters.

$$F_{\text{impact}} = m a_{\max} \tag{3.15}$$

the $x_{\max}$ parameter is the oscilation amplitude. Assuming a radial oscilation mixer, this parameter is given as

$$x_{\max} = \frac{L}{2} \tag{3.16}$$

the mass of the ball can be calculated uising the ball density

$$m = \rho\frac{4}{3}\pi r^3 \tag{3.17}$$

$$F_{\text{impact}} = \frac{2}{3}\rho\pi r^3 L \cdot (2\pi f_{\text{mill}})^2 \tag{3.18}$$

this way,

$$\sigma = \left(\frac{6}{\pi^3}\frac{E^{*2}}{r^2}\frac{2}{3}\rho\pi r^3 L \cdot (2\pi f_{\text{mill}})^2\right)^{1/3} \tag{3.19}$$

Therefore, it is possible to get

$$\boxed{\sigma = \left(16 E^{*2} r \rho L f_{\text{mill}}^2\right)^{1/3}} \tag{3.20}$$

One of the most easily changeable parameters in mechanochemestry is the mill frequency. Therefore, it is usefull to define σ in terms of it and take the other paremeters as constants

$$\boxed{\sigma = C_{\text{ball}}^{\text{mill}} f^{2/3}} \tag{3.21}$$

this stabilishes an important relationship.

3.3.2 The reduced Young's Modulus (E^*)

The reduced Young's modulus, E^*, accounts for the elastic properties (Young's modulus E_i and Poisson's ratio μ_i) of both colliding bodies. Those are stiffness and elastic properties that can be obtained from computational methods using the elastic tensor.

$$\frac{1}{E^*} = \frac{1-\mu_1^2}{E_1} + \frac{1-\mu_2^2}{E_2} \tag{3.22}$$

In our system, two types of collisions are most important:

1. Ball-crystal collisions (ball vs. coformer A or B).
2. Crystal-crystal collisions (coformer A vs. coformer B).

A rough estimative, that is proposed here, is to compute those modules pair-wise between coformer A and the ball (E_A^*), cofformer B (E_B^*)and the ball. After this, the reduced modules is recalculated using the already reduced one:

$$\frac{1}{E_i^{\circledast}} = \frac{1-\mu_i^2}{E^*} + \frac{1-\mu_{j\neq i}}{E_j} \tag{3.23}$$

and them use a weighted avarege for the reduced Young's Modulus

$$E_{\text{effective}}^* = \eta_A \cdot E_A^{\circledast} + \eta_B \cdot E_B^{\circledast} \tag{3.24}$$

Being η_i molar propotions.

3.3.3 Modeling reaction kinetics

Using 3.3 it is possible to get the reaction rate k:

$$k = A\exp\left(-\frac{E_{\text{act}}}{k_B T} + \frac{C_{\text{ball}}^{\text{mill}}\Delta V^{\ddagger} f_{\text{mill}}^{2/3}}{k_B T}\right) \tag{3.25}$$

this is very interesting because it gives a lower limit for reaction. Let's suppose the activation energy is 0, then the rate only depends on interactions and the system is very close to an spontaneous reaction.

In a spontaneous system, $k = A$. Therefore, it is clear that interesting experimental details can be optimized in this system

$$E_{\text{act}} = C_{\text{ball}}^{\text{mill}} \Delta V^{\ddagger} f_{\text{mill}}^{2/3} \tag{3.26}$$

$$\boxed{f_{\text{mill, min}} = \left(\frac{E_{\text{act}}}{C_{\text{ball}}^{\text{mill}} \Delta V^{\ddagger}} \right)^{3/2}} \tag{3.27}$$

This is the most important and easily testable hypothesis of this work. The minimum frequency for activation, should be proportional to the activation energy to the power of $\frac{3}{2}$ $\left(f_{\text{mill, min}} \propto E_{\text{act}}^{3/2} \right)$. This relationship can also be visualized on fig 3.4

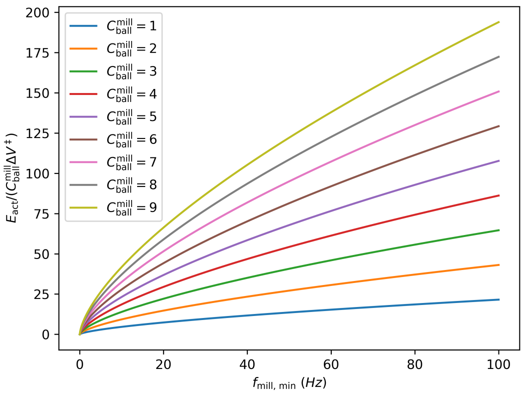

Figure 3.4: Activation energy vs minimum milling frequency with arbitrary units for $C_{\text{ball}}^{\text{mill}}$,

3.3.4 Discussion

The main problem with this work is that the activation energy is considered as constant. It isn't. In mechanochemical processes, crystals are damaged, creating defects that act as preferential reaction points. Senna, M. *et. all*[7] mention this problem. This method could still be used for faster reactions, as there would be no time for crystal degradation to be a significant factor.

Another error in approximation is that, Senna, M. also argues that maybe the ΔG of the crystal shouldn't be the one at rest, but the one when the crystal is deformed by contact. This is a valid point, but this model should first be proven to work before being improved further. With no experimental evidence, it is pointless to pick at details.

It would be probably more productive to model an empirical law of how crystals usually decay, but that would only be valid for specific types of crystals. Harder crystals would probably be more brittle, generating smaller pieces and pieces that don't break cleanly in the habit surface. That would probably result in a smaller activation energy.

The model could maybe be improved by adding an energy decay parameter that decays linearly with time, but it also would need to depend on the relative concentration of product and reagents.

3.4 Conclusion

This work opens a path to optimize experimental parameters to obtain co-crystals in a better and faster way. Its formalism is generic enough that this should work for normal (covalent or ionic) mechanochemical reactions given that the elastic tensors can be calculated. It also provides the proportionality relationship from milling frequency to activation energy $\left(f_{\text{mill, min}} \propto E_{\text{act}}^{3/2} \right)$.

This is also useful if there is a need to produce a compound that isn't the most stable possible, but has better properties, by limiting the frequency between ${E_{\text{act}}^{1}}^{3/2} < C^{*} f_{\text{mill, min}} < {E_{\text{act}}^{2}}^{3/2}$ (C^{*} being defined as $(C_{\text{ball}}^{\text{mill}} \Delta V^{\ddagger})^{-1}$), as it is noted that if something doesn't exist naturally but is more stable, it usually has a higher activation energy.

This work is still missing the most important step, experimental validation. As custom built equipment is necessary, there was no time to do it until the due date. But it is a good framework for building future improvements on.

Bibliografia

[1] Co-crystal - Online Dictionary of Crystallography [WWW Document], n.d. URL https://dictionary.iucr.org/Co-crystal (accessed 8.18.24).

[2] Fischer, F., Wenzel, K.-J., Rademann, K., Emmerling, F., 2016. Quantitative determination of activation energies in mechanochemical reactions. Physical Chemistry Chemical Physics 18, 23320–23325. https://doi.org/10.1039/C6CP04280E

[3] H. Hergesell, A., L. Seitzinger, C., Burg, J., J. Baarslag, R., Vollmer, I., 2025. Influence of ball milling parameters on the mechano-chemical conversion of polyolefins. RSC Mechanochemistry 2, 263–272. https://doi.org/10.1039/D4MR00098F

[4] Zhang, R., Zeitler, A., 2025. Mechanochemical Cocrystallisation in a Simplified Mechanical Model: Decoupling Kinetics and Mechanisms Using THz-TDS. https://doi.org/10.26434/chemrxiv-2025-nrk7j

[5] Andersen, J.M., Mack, J., 2017. Decoupling the Arrhenius equation via mechanochemistry. Chem. Sci. 8, 5447–5453. https://doi.org/10.1039/C7SC00538E

[6] Boscoboinik, A., Olson, D., Adams, H., Hopper, N., Tysoe, W.T., 2020. Measuring and modelling mechanochemical reaction kinetics. Chem. Commun. 56, 7730–7733. https://doi.org/10.1039/D0CC02992K

[7] Senna, M., L. Michalchuk, A.A., 2025. Reassessing mechanochemical processes in polyatomic systems for smart fabrication of nanocomposites. RSC Mechanochemistry 2, 351–369. https://doi.org/10.1039/D4MR00084F

4

The Bose-Einstein condensation

Matheus Aleluia Rodrigues

Instituto de Física de São Carlos, Universidade de São Paulo, 13560-970 São Carlos, SP, Brazil

Abstract: The fundamental ideas behind quantum mechanics have been extensively studied since the beginning of the 20th century. These foundations explore how we can understand the remarkable and often non-intuitive nature of the microscopic world. The states provided by Bose-Einstein condensates approach this previously mentioned idea. Under such circumstances, these states allow us to observe quantum effects on scales that we were not previously able to recognize in macroscopic systems. In this article, we will address this perspective, starting with the statistical description, theoretical background, and experimental applications.

4.1 Introduction

More than one century ago, an idea was proposed by Bose to describe how "*light quanta*" (photons) can be divided into "cells" whose volume has units of h^3 [1], and through which thermodynamic properties of radiation could recovered macroscopically. A link between thermodynamics and quantum mechanics was created by this discovery, without any previously classical theory being used. In his paper, it was analyzed how the energy distribution in black bodies, as proposed by Planck and suggested by Einstein, can be related to the exchange of energy between particles and molecules, based on elementary principles following Planck's formalism [2].

Uncountable reasons can be traced to Einstein's contributions to quantum mechanics, but also his efforts to quantum statistics must certainly be mentioned. In three papers published between 1924 and 1925 [3, 4, 5], ideas were presented that, when connected to the aforementioned description by Bose, led to the establishment of what is now called the Bose-Einstein distributions and are directly related to Bose-Einstein condensate (BEC). In his paper it brought the quantization of ideal gas, which means, the quantization of free massive particles that is clearly a manifestation of quantum statistics.

Bose-Einstein condensation (BEC) was experimentally achieved in the mid-1990s in dilute atomic gases of rubidium [6], sodium [7], and lithium [8], providing a unique opportunity to study a quantum state on a macroscopic scale. This new state of matter, known as a *superfluid*, offered a different perspective on the microscopic world and revealed distinct experimental features. The high densities of these systems allow for a description in terms of a single wavefunction, with all atoms in the sample occupying the same quantum state. In the following sections, we present a brief theoretical introduction to BEC, along with the fundamental techniques used to reach the ultracold temperatures necessary for its realization.

4.2 Bose-Einstein distribution for microcanonical states

4.2.1 Indistinguishable particles

The microscopic quantum world requires a description based on the states energy, volume, and number of particles, but the description presented so far only accounts for the multiple combinations of microstates that may constitute the same macrostate. It is necessary to deal with what is referred to as *indistinguishable particles*, in particular, *bosons*. Here, we will consider only the case of bosons; the fermion case can be found in [12, 14]. The description can be done in different ways in which the particles N can be organized into m "cells" with n_j elements. However, now the particles cannot be distinguished by their permutations, and consequently, the analysis must be modified. This problem emerges when the phase space is quantized, assuming that the size of each cell cannot be small enough to group just a particle - following this idea does not make sense in quantum statistics. With the purpose of accounting indistinguishable particles, it is necessary to rewrite the partition function to include all cases that may arise, i.e., allowing a general way to reorganize the particles n_j within the same box j, with g_j sub-cells, all having the same energy ε_j, providing different possible ways to fill the j-th cell . The key to understanding this process is the concept of *degeneracy*. [14].

$$n_j = \frac{g_j}{e^{\beta(\varepsilon_j - \mu)} - 1}, \tag{4.1}$$

where $\beta = \frac{1}{k_B T}$, ε is energy and μ is the chemical potential. In Fig. 4.1 is showed the Bose-Einstein distribution for differents *fugacities*, defined as $Z = e^{\beta\mu}$.

4.3 Density of states

When evaluating the thermodynamic properties of gases, it is common to replace sums over states by integrals, using the concept of density of states, in which the energy level structure is treated as continuous. In general, however, for the purposes of this paper, such an approach fails due to the significant contribution of the low-energy states, which are not adequately captured in this approximation, although it provides a good description of the contributions from excited states [10]. Since studies are generally based on gases confined in trapping potentials, it is of great interest to investigate the influence of the environment on these atoms. As the atoms are trapped in various types of potentials ($U(\mathbf{r})$), non-homogeneous behaviors can be observed as a consequence, meaning that the distribution of available particles varies in space. In the general case, the Hamiltonian in three dimensions can be written as:

$$\hat{H} = \frac{-\hbar^2}{2m}\nabla^2 + U(\mathbf{r}) \tag{4.2}$$

As a consequence of trapping potential, the wave function is localized and all states have discrete energy levels, with the atomic population determined by these levels. As mentioned earlier, some levels are degenerate, and the way the atomic cloud is organized is governed by the trapping potential through the *density of states* $\eta(\epsilon)$. For an arbitrary potential, the density of states is given by:

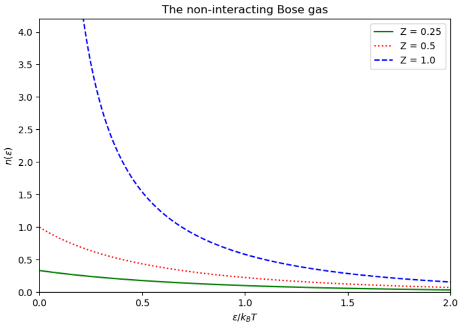

Figure 4.1: Bose-Einstein distribution for different values of fugacity Z in terms of $\epsilon/k_B T$.

$$\int \eta(\epsilon) d\epsilon = \frac{(2m)^{3/2}}{(2\pi)^2\hbar^3} \int d^3r \int d\epsilon \sqrt{\epsilon - U(\mathbf{r})}, \tag{4.3}$$

but frequently is seen the harmonic case, written as:

$$\eta(\epsilon) = \frac{\epsilon^2}{2(\hbar\bar{\omega})^3}. \tag{4.4}$$

where, ϵ is energy and $\bar{\omega}$ is mean frequency.

4.4 Bose-Einstein condensate

4.4.1 Condensation of a harmonically confined ideal gas

The Bose-Einstein condensate in a non-interacting gas of bosons is treated in several books on quantum statistics and represents the most well-known case in which quantum effects can be observed on a macroscopic scale. The theory presented can also be applied to quantum phenomena involving atomic interactions, such as helium superfluidity. Below will be discussed the conditions under which the Bose-Einstein condensate occurs.

When the kinetic energy of a bosonic gas decreases, is directly related to a reduction in its temperature. Under such a regime, it is expected that the atoms occupy the lowest energy level, i.e., $\epsilon_{j=0} = 0$, of the trapping potential. In the grand canonical ensemble the number of particles can be written as:

$$n_j = -\frac{\partial\Omega}{\partial\mu} = w_{T,\mu}(\varepsilon_j), \tag{4.5}$$

where Ω is the Landau potential, and $w_{T,\mu}$ is the statistical distribution function. At low temperatures, with the system maintained in the ground state, this equation becomes [12]:

$$n_0 \overset{\varepsilon_0 \to 0}{\to} w_{T,\mu}(0) = \frac{1}{1/Z - 1} = N, \tag{4.6}$$

where Z is the *fugacity*. The equation above matches (4.1), except for the degeneracy factor g_j, which is expressed in terms of the density of states.

In the thermodynamic limit, i.e., as $N \to \infty$, the system is observed from a macroscopic perspective, and the fugacity approaches its maximum value, $Z \to 1$. It expresses a macroscopic condition for the ground state population and allows us to calculate the population that composes this state. For a specific gas with a large number of particles, whose energy spectrum is given by $\epsilon = \frac{p^2}{2m}$, the density of states is given by [12]:

$$\eta(\epsilon) = \frac{(2m)^{3/2}}{(2\pi)^2\hbar^3} V\sqrt{\epsilon}, \tag{4.7}$$

and using (4.5), Boltzmann distribution appears in the thermodynamic limit presenting the total number of atoms in ground state:

$$N = \int_0^\infty \eta(\epsilon) w_{T,\mu}(\epsilon) d\epsilon = \frac{V}{\lambda_{\mathrm{th}}^3} g_{3/2}(Z), \tag{4.8}$$

where g is *Bose function*[1] and λ_{th} is the thermal de Broglie wavelength [12].

The values of Bose distribution are limited by phase space $g_{3/2}(0) \to g_{3/2}(1)$. When $T \to 0$, de Broglie wavelength diverges, but $g_{3/2}$ is limited. As consequence to Bose distribution, the *fugacity*, when $Z \overset{T \to 0}{\to} 1$, result in the number of atoms going to zero at lowest energy state. The previously cited consequence caused by replacing sums integrals and the chemical potential is limited by the minimal energy level [10]. In this levels the density of states disappears and is necessary to establish a discrete term to join again the lowest level as solved by Einstein. Thus the population is given by:

$$N = N_c + \frac{V}{\lambda_{\mathrm{th}}^3} g_{3/2}(Z), \tag{4.9}$$

if the number of particles in excited states is less than N, the remaining particles must be arranged in the single ground state, whose occupation number can become possibly large. Thus, the system exhibits a *Bose-Einstein condensate.*

In this context is necessary to do a separation between the ground state and remnants levels (excited) analyzing the temperatures that differs these two situations - as know as *critical temperature* T_c. This temperature plays a significant role in the system, as it represents the minimum value below which atoms begin to condense. When the system temperature $T > T_c$, all atoms are well distributed among the available states; each state has its own population, meaning the distribution is uniform and the states are sparsely populated, i.e. $N_c = 0$.

When the system temperature $T \leq T_c$, the excited states can no longer accommodate all the particles. As a result, the surplus particles begin to accumulate in the ground state, leading to a macroscopic occupation when $\mu \to 0$. This marks the onset of the Bose-Einstein condensate, where a finite fraction of the total particles resides in the lowest energy level. With $\mu = 0$ and the temperature fixed at T_c, the number of particles in excited states becomes steady and temperature-independent. Thus, N is given by:

$$N = \frac{V}{\lambda_{\mathrm{c}}^3} g_{3/2}(1), \tag{4.10}$$

where λ_{c} is defined at T_c. Then T_c is obtained:

$$T_c = \frac{2\pi\hbar^2}{k_B m} \left(\frac{N}{V g_{3/2}(1)} \right)^{2/3}. \tag{4.11}$$

Normalizing by the total number of particles and using the relation above, it is possible to write[2]:

$$\boxed{\frac{N_c}{N} = 1 - \left(\frac{\min(T, T_c^{(3/2)})}{T_c^{(3/2)}} \right)^{3/2}} \tag{4.12}$$

4.4.2 Density and momentum distribution for a Bose gas

One of the characteristics of cold/ultra-cold atoms systems is the number of confined particles, when the temperature is around the microkelvin scale. Under this regime, the atomic cloud often contains between 10^4 and 10^7 atoms. This number quickly decreases by fractions due to the different techniques used for trapping and cooling the system, and it is possible to relate this behavior to two fundamental reasons. First, the system is metastable, so interaction with other species is not possible in equilibrium. Second, the system's lifetime is on the order of seconds, or at most, minutes [10].

---

[1] The Bose function here is describe in therms of integral representation and can be find at [10, 12, 14]

[2] It is important to explain that the particle distribution depends on the type of potential. Here, for a box potential.

These quantities can be related by measuring the density profile. In principle, two different types of imaging are used to obtain this distribution: absorption imaging and phase-contrast imaging. The first one is not useful for a Bose-Einstein condensate due to the high optical density close to T_c [17]; however, phase-contrast imaging is a good option because is almost non-destructive and is possible to evaluate the same cloud of these systems.

In inhomogeneous potentials, the normal fraction and the condensate occupy different energy levels and form spatially separated clouds, with the condensate being concentrated around the center of the potential in a dense form. If the atomic cloud is allowed to expand, its distribution depends not only on the initial density distribution, but also on the velocity distribution, given by [12]:

$$\begin{aligned} n(\mathbf{x}) &= \frac{1}{\lambda_{\text{th}}^3}\, g_{3/2}\left(e^{-\beta[U(\mathbf{x})-\mu]}\right) \\ n(\mathbf{k}) &= \frac{a_{\text{ho}}^6}{\lambda_{\text{th}}^3}\, g_{3/2}\left(e^{\beta\left(\mu-\frac{\mathbf{p}^2}{2m}\right)}\right), \end{aligned} \tag{4.13}$$

where a_{ho} is the spatial extend of ground state of the harmonic oscillator, given by $a_{\text{ho}} = \sqrt{\hbar/m\omega}$.

4.4.3 Real BEC

The Bose-Einstein condensate occurs when some atoms share the same lowest energy quantum state. Below the critical temperature, a separation can be observed between two different spatial distributions (condensate and normal), as well as in the momentum distributions. It is important to cite that this description applies to an ideal gas, where particles do not interact, however in inhomogeneous gases, it is necessary to evaluate the collisions among the atoms that compose the cloud and reformulate formalism to describe these collisions in order to understand their thermodynamic behavior. In order to obtain low temperatures and high densities for a gas of atoms characterizing a BEC, a phase transition must occur when the spatial density described by (4.13) satisfies the condition $n\lambda_{\text{th}}^3 \geq 2.612$. Due the cooling process is possible to achieve μK temperatures with small loss of atoms, so that the phase space density can be increased. However, this increase by a laser cooling of alkali atoms had reached its limit by Doppler limit and BEC was not formed yet. If the density increases, light scattered by one atom is absorbed by others, causing a heat and repulsion between them.

A promising way to achieve BEC is via evaporative cooling[3]. This technique consists of the preferential removal of atoms from a confined sample that have higher-than-average energy, followed by the rethermalization of the remaining gas through elastic collisions [16]. This procedure is based on *scattering theory*, and the solution for such systems is obtained using *partial-wave analysis*. At large interparticle distances, where the potential energy $V(R)$ becomes negligible compared to the total energy E, the wavefunctions reduce to simple oscillatory forms. In this regime, the solutions of the Schrödinger equation in the absence of the potential term $V(R)$ can be used, differing only by a phase shift δ_l between them [16]. Both the differential and total cross-sections can be expressed in terms of these phase shifts, and the total cross-section is given by:

$$\sigma = \frac{4\pi}{k^2}\sum_{l}^{\infty}(2l+1)\sin^2\delta_l, \tag{4.14}$$

where $k = \sqrt{2ME}/\hbar$ is the wavevector, l is partial waves given by coefficients of Legendre polynomials and δ_l is phase shift.

As the most energy particle was evaporated to the trap, those that remain have much lower average energy, occupying a small volume around the center of trap, thereby increasing the density.

Elastic collisions drive the thermalization process of the gas after the trap depth has been lowered, and this effect can be enhanced by using a large cross-section. On the other hand, inelastic collisions produce a acceleration in the particles, which can then reach high energies to remain trapped. These collisions can be described by one parameter, named *scattering length a*. At ground state only the phase shift δ_l for $l = 0$ is important. Thus, the description can be understood as: the wavefunction in the inner range of the potential is no longer dependent on the energy of collision, since the potential is much larger than the collision energy. Under these condictions is possible to define the scattering lenght as [16]:

$$a = -\lim_{k\to 0}\frac{\delta_0}{k}. \tag{4.15}$$

For the BECs, a plays a primordial role.

As previously described, particles do interact, and a widely used and elegant way to handle this is by using the lowest-order approximation, in which the interaction takes the form of a mean-field repulsive force. In this case, the Hamiltonian assumes a non-linear term due to the interaction, which is responsible for the collisions/interactions and is proportional to the local density of atoms, denoted by V_{int}. Since the local density is itself $|\psi|^2$, this makes

---

[3] See details in *Laser Cooling and Trapping* [16]

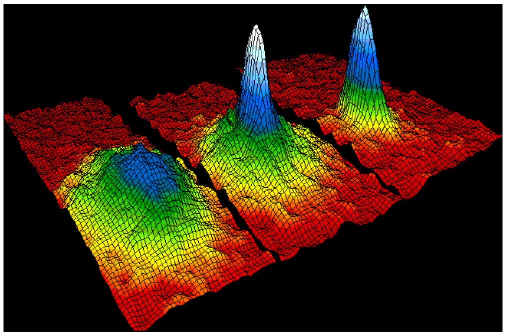

Figure 4.2: Spatial distributions found and taken from Cornel and Wienan after release from trap [6].

the Schrödinger equation for atomic motion result in the *Gross-Pitaevskii equation*[16], being for N atoms:

$$\left[-\frac{\hbar^2}{2m}\nabla^2 + V_{\rm t}(\mathbf{R}) + NV_{\rm int}|\Psi(\mathbf{R})|^2\right]\Psi(\mathbf{R}) = E_N\Psi(\mathbf{R}) \tag{4.16}$$

where $\mathbf{R}$ is the coordinate of an atom in the trap, $V_{\rm t}$ is the trapping potential that confines the atoms, and $V_{\rm int} = 4\pi\hbar^2 a/M$ is the coefficient related to the mean-field interaction between the atoms. We can analyze the role described by the scattering length in the following way: if $a > 0$, the interaction is repulsive, so the BEC tends to disperse. It is related by the harmonic potential that traps the atoms in the ground state, resulting in a wavefunction that is somewhat more spread out and flatter than a Gaussian. On the other hand, for $a < 0$, the interaction is attractive and the BEC eventually forms a wavefunction that maintains a Gaussian shape, as expected by the harmonic potential [16].

The solution of (4.16) describes that all condensate atoms share the same wavefunction, and increasing the number of atoms in the condensate does not increase its volume. This equation and its *posteriori* consequences predicting condensation are indeed profound outcomes. If atoms in a trap or a bound container satisfies the above equation, then a fraction of these atoms will be in the lowest energy level, whose wavecfunction spans a amount of the accessible volume.

]

4.5 Road away for Bose-Einstein condensate

The first attempt to recognize and realize Bose-Einstein condensation (BEC) is associated with phase transitions in ^{4}He observed in the late 1930s. ^{4}He satisfies equation (4.16) at high temperatures (around 2.2 K), and its properties change drastically at this point, exhibiting superfluid behavior. However, because helium becomes a strongly interacting liquid with zero viscosity, only a small fraction (about 10%) of the atoms actually enter the condensate. This limitation is related to the tendency of two hydrogen atoms to recombine into an H_2 molecule, which was initially thought to prevent BEC due to the rarity of the required three-body collisions. Nonetheless, with the development of evaporative cooling techniques, a BEC in atomic hydrogen was finally achieved in 1998 by Fried *et al.* [18].

The first experimental realization of BEC in an alkali vapor was achieved in 1995 by Cornell and Wieman *et al.*[6], who used a combination of laser cooling and magnetic trapping techniques on a cloud of ^{87}Rb atoms. Approximately four months later, an independent team led by Ketterle *et al.*[7] produced a BEC in ^{23}Na. A key difference between these two experiments was the number of atoms: Ketterle's team achieved a condensate containing about a hundred times more atoms, which enabled the observation of distinct quantum effects such as matter-wave interference [9], as showed in Fig.4.3. For their groundbreaking contributions, Cornell, Wieman, and Ketterle were awarded the Nobel Prize in Physics in 2001.

Achieving BEC required multiple cooling stages. Initial cooling methods, such as optical molasses or a magneto-optical trap (MOT), typically resulted in atom densities of approximately 10^{10} atoms/cm^3. However, BEC requires densities between 10^{11} and 10^{15} atoms/cm^3, making evaporative cooling a crucial step in reaching the required phase-space density. The standard method to detect a Bose-Einstein condensate (BEC) involves a carefully designed apparatus that allows for measuring the spatial distribution of atoms after a short delay time following their release from the trapping potential. One common approach is to perform ballistic expansion measurements—that is, to analyze the atomic distribution after a time-of-flight. This distribution is then used to infer the velocity distribution of the atoms in the original sample based on the observed spatial profile. The Fig. 4.2 shows he spatial distributions of atoms after release from trap, using ballistic parameters is possible to obtain the size of the cloud, shape and velocity distribution.

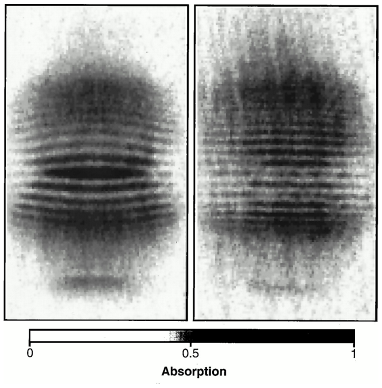

Figure 4.3: Mater-waves interference in BEC produced by Andrews, *et al.* [9].

4.6 Conclusion

The purpose of this paper was to explore and understand various concepts and techniques related to the realization of Bose-Einstein condensates (BEC), including the experimental methods and the statistical and quantum foundations that define a BEC. The theoretical background acquired throughout this work enabled a deeper understanding of the role of the ideal gas model and how real systems deviate from this idealization. I would like to thank Dalila Riviero for her valuable insights and discussions on the conditions for BEC and related topics.

Bibliografia

[1] Bose, S. Plancks Gesetz und Lichtquantenhypothese. *Zeitschrift für Physik* **26**, 178–181 (1924)

[2] Planck, M. *The theory of heat radiation*. (Blakiston, 1914)

[3] Einstein, A. Quantentheorie des einatomigen idealen Gases. *Königliche Preußische Akademie der Wissenschaften. Sitzungsberichte*, 261–267 (1924)

[4] Einstein, A. Quantentheorie des einatomigen idealen Gases. Zweite Abhandlung. *Sitzungsberichte der Preußischen Akademie der Wissenschaften (Berlin). Physikalisch-mathematische Klasse*, 3–14 (1/925)

[5] Einstein, A. Zur Quantentheorie des idealen Gases. *Sitzungsberichte der Preußischen Akademie der Wissenschaften (Berlin). Physikalisch-mathematische Klasse*, 18–25 (1925)

[6] M. H. Anderson and J. R. Ensher and M. R. Matthews and C. E. Wieman and E. A. Cornell. Observation of Bose-Einstein Condensation in a Dilute Atomic Vapor. Science

[7] Davis, K. B., Mewes, M.-O., Andrews, M. R., van Druten, N. J., Durfee, D. S., Kurn, D. M. & Ketterle, W. Bose–Einstein condensation in a gas of sodium atoms. *Phys. Rev. Lett.* **75**, 3969–3973 (1995)

[8] Bradley, C. C., Sackett, C. A. and Hulet, R. G. Bose-Einstein condensation of lithium: Observation of limited condensate number. *Phys. Rev. Lett.* **78**, 985–989 (1997). doi:10.1103/PhysRevLett.78.985

[9] Andrews, M. R. *et al.* Observation of interference between two Bose condensates. *Science* **275**, 637–641 (1997). doi:10.1126/science.275.5300.637

[10] Pethick, C. J. & Smith, H. *Bose–Einstein Condensation in Dilute Gases*. 2nd ed. (Cambridge University Press, 2008)

[11] Pérez, E. & Sauer, T. Einstein's quantum theory of the monatomic ideal gas: non-statistical arguments for a new statistics. *Archive for History of Exact Sciences* **64**, 561–612 (2010)

[12] Courteille, Ph. W. *Thermodynamics and Statistical Physics for Material Sciences and Quantum Gases*. (IFSC-USP, 2025 s.d.)

[13] Callen, H. B. *Thermodynamics and an Introduction to Thermostatistics*. 2nd ed. (John Wiley & Sons, 1980)

[14] Huang, K. *Statistical Mechanics*. (John Wiley & Sons, 2008)

[15] Landau, L. D. & Lifshitz, E. M. *Statistical Physics: Volume 5*. (Elsevier, 2013)

[16] Metcalf, H. J. & Van der Straten, P. *Laser Cooling and Trapping*. (Springer Science & Business Media, 1999)

[17] Andrews, M. R., Mewes, M.-O., van Druten, N. J., Durfee, D. S., Kurn, D. M. & Ketterle, W. Direct, Nondestructive observation of a Bose condensate. *Science* **273**, 84–87 (1996)

[18] Fried, D. G. *et al.* Bose-Einstein condensation of atomic hydrogen. *Phys. Rev. Lett.* **81**, 3811–3814 (1998). doi:10.1103/PhysRevLett.81.3811

5

The free electron gas model

Vinícius Bastos Marcos

Instituto de Física de São Carlos, Universidade de São Paulo, 13560-970 São Carlos, SP, Brazil

Abstract: The free electron gas model represents a foundational, albeit simplified, approach in condensed matter physics for understanding the electronic properties of metals. This paper provides a comprehensive review of the model, from its quantum mechanical formulation to its key successes and ultimate limitations. Beginning with the particle-in-a-box problem, we derive fundamental concepts for the three-dimensional electron gas, including the Fermi energy, the density of states, and the Fermi-Dirac distribution. We then demonstrate the model's predictive power by showing how it successfully accounts for the linear temperature dependence of the electronic heat capacity and provides a theoretical basis for the empirical Wiedemann-Franz law. Subsequently, we analyze the model's significant failures. These include its inability to distinguish between metals, semiconductors, and insulators; its failure to explain positive Hall coefficients observed in some metals; and the paradox of unrealistically long electron mean free paths. In conclusion, while the free electron model provides crucial insights, its shortcomings underscore the essential role of the crystal's periodic potential, motivating the transition to the more complete framework of band theory.

5.1 Introduction

The quest to understand the behavior of electrons in solids is a cornerstone of modern condensed matter physics. It is the key to understanding a vast array of material properties, from electrical and thermal conductivity to magnetism and optical characteristics. One of the earliest and most successful attempts to model this complex many-body problem is the **free electron gas model**.

Proposed initially by Drude and later refined by Sommerfeld, who incorporated quantum mechanics, this model provides a powerful, albeit simplified, picture of metallic solids. It treats the valence electrons as a gas of non-interacting fermions, free to move within the confines of the crystal lattice. The lattice's complex potential is radically simplified to a uniform potential box. This approximation, despite its simplicity, allows for the derivation of several fundamental properties of metals with surprising accuracy.

This paper will explore the theoretical framework of the free electron gas model. We will begin by solving the Schrödinger equation for electrons in a one-dimensional potential well and extend this to the three-dimensional case using periodic boundary conditions. This will allow us to derive fundamental quantities like the **Fermi energy** and the **density of states**. We will then introduce the **Fermi-Dirac distribution** to account for thermal effects. We will examine the model's successes, such as its explanation of Ohm's law and the Wiedemann-Franz law, and delve into its notable limitations, including its inability to explain the electronic heat capacity at low temperatures or the existence of insulators and semiconductors. By analyzing both its triumphs and shortcomings, we aim to provide a comprehensive understanding of this foundational model and its crucial role in paving the way for more sophisticated theories, such as band theory.

5.2 The 1D quantum well: A starting point

In quantum mechanics, the "particle in a box" is a foundational problem. We begin with this simple case to build our intuition. Consider a single electron of mass m confined to a one-dimensional box of length L. We model this with a potential $V(x)$

that is zero inside the box and infinite outside:

$$V(x) = \begin{cases} 0 & 0 < x < L \\ \infty & \text{otherwise} \end{cases}$$

Inside the box, the Hamiltonian $\hat{H}$ contains only the kinetic energy term. The time-independent Schrödinger equation is:

$$\hat{H}\psi_n(x) = -\frac{\hbar^2}{2m}\frac{d^2\psi_n(x)}{dx^2} = E_n\psi_n(x) \qquad (5.1)$$

The boundary conditions, $\psi_n(0) = \psi_n(L) = 0$, dictate that the solutions must be standing waves. The normalized wavefunctions are:

$$\psi_n(x) = \sqrt{\frac{2}{L}}\sin\left(\frac{n\pi x}{L}\right) \qquad (5.2)$$

where $n = 1, 2, 3, \dots$ is a positive integer quantum number. Substituting this solution back into the Schrödinger equation yields the quantized energy levels:

$$E_n = \frac{\hbar^2 k_n^2}{2m} = \frac{\hbar^2\pi^2}{2mL^2}n^2 \qquad (5.3)$$

Now, let's place N non-interacting electrons into this 1D box. Since electrons are fermions, they must obey the **Pauli Exclusion Principle**: no two electrons can occupy the same quantum state. A state is defined by the quantum number n and the spin projection ($m_s = \pm 1/2$). Therefore, each energy level E_n can hold a maximum of two electrons, one with spin up and one with spin down.

At absolute zero ($T = 0$), the electrons fill the lowest available energy levels. If we have N electrons, they will fill the first $N/2$ orbital states (assuming N is even). The quantum number of the highest occupied level is thus $n_F = N/2$. The energy of this topmost level is, by definition, the **Fermi Energy (E_F)**.

$$E_F = \frac{\hbar^2\pi^2}{2mL^2}\left(\frac{N}{2}\right)^2 = \frac{\hbar^2\pi^2 N^2}{8mL^2} \qquad (5.4)$$

This simple 1D result already shows that due to the Pauli principle, the energy of the most energetic electron can be very large, a key insight that classical physics misses.

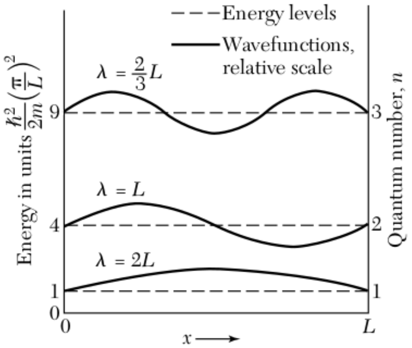

Figure 5.1: Quantized energy levels of an electron confined in a one-dimensional box. Each level can be occupied by two electrons with opposite spins. [1]

5.3 The 3D free electron gas

To model a real solid, we extend our analysis to three dimensions. While we could use infinite potential walls as in the 1D case, it is mathematically more convenient to use **periodic (Born-von Karman) boundary conditions**. This assumes our cube of side L is part of an infinite, repeating lattice, which effectively removes surface effects. This approach is justified because for a macroscopic crystal, the number of atoms on the surface is negligible compared to the number in the bulk.

Periodic boundary conditions favor traveling plane wave solutions for the wavefunction:

$$\psi_{\vec{k}}(\vec{r}) = \frac{1}{\sqrt{V}}e^{i\vec{k}\cdot\vec{r}} \qquad (5.5)$$

where $V = L^3$ is the volume of the box and $\vec{k}$ is the wave vector. The boundary condition $\psi(x + L, y, z) = \psi(x, y, z)$ (and similarly for y and z) restricts the allowed values of $\vec{k}$:

$$k_x = \frac{2\pi n_x}{L}, \quad k_y = \frac{2\pi n_y}{L}, \quad k_z = \frac{2\pi n_z}{L} \qquad (5.6)$$

where n_x, n_y, n_z are any integers (positive, negative, or zero). These allowed $\vec{k}$ vectors form a discrete grid in a reciprocal space known as **k-space**. Each point on this grid represents a distinct orbital state.

The energy of an electron in a state $\vec{k}$ is found by substituting the plane wave into the 3D Schrödinger equation:

$$E_{\vec{k}} = \frac{\hbar^2 k^2}{2m} = \frac{\hbar^2}{2m}(k_x^2 + k_y^2 + k_z^2) \qquad (5.7)$$

5.3.1 The Fermi sphere and Fermi energy

At $T = 0$, the N electrons fill the lowest energy states, which correspond to the k-space points closest to the origin ($\vec{k} = 0$). The filled states form a sphere in k-space, known as the **Fermi sphere**. Its radius is the **Fermi wave vector (k_F)**, and its surface is the **Fermi surface**. All states with $|\vec{k}| < k_F$ are occupied, and all states with $|\vec{k}| > k_F$ are empty.

To find k_F, we count the total number of states within this sphere. The volume of a single state in k-space is $\left(\frac{2\pi}{L}\right)^3$. The total number of orbital states inside the Fermi sphere is its k-space volume divided by the volume per state:

$$N_{\text{states}} = \frac{\text{Volume of Fermi Sphere}}{\text{Volume per State}} = \frac{\frac{4}{3}\pi k_F^3}{(2\pi/L)^3} = \frac{V}{6\pi^2}k_F^3 \tag{5.8}$$

Since each state can hold two electrons (spin up and spin down), the total number of electrons N is:

$$N = 2 \times N_{\text{states}} = \frac{V}{3\pi^2}k_F^3 \tag{5.9}$$

We can now express the Fermi wave vector k_F in terms of the electron density $n = N/V$:

$$k_F = (3\pi^2 n)^{1/3} \tag{5.10}$$

The **Fermi energy (E_F)** is the energy corresponding to k_F:

$$E_F = \frac{\hbar^2 k_F^2}{2m} = \frac{\hbar^2}{2m}(3\pi^2 n)^{2/3} \tag{5.11}$$

This is one of the most important results of the free electron model. It shows that the maximum kinetic energy of an electron in a metal depends only on the electron density. For typical metals like copper, E_F is on the order of 7 eV, an enormous energy corresponding to a temperature of about 80,000 K. This explains why electrons contribute very little to the heat capacity of a metal at room temperature—only those very near the Fermi surface can be thermally excited.

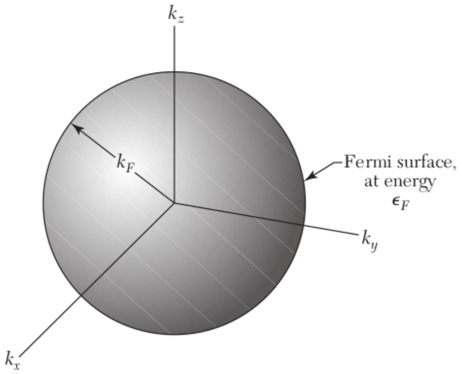

Figure 5.2: A conceptual illustration of k-space at T=0. The discrete points represent allowed electron states. The electrons fill all states within the Fermi sphere (radius k_F), which has an associated energy E_F. The states outside the sphere are empty. [1]

5.4 Density of states and the Fermi-Dirac distribution

To understand the thermal properties of the electron gas, we need two key concepts: the **density of states**, which tells us how many states are available at a given energy, and the **Fermi-Dirac distribution**, which tells us the probability of those states being occupied.

5.4.1 Density of states (DOS)

The density of states, $g(E)$, is defined as the number of available electronic states per unit volume, per unit energy range. We can derive it by starting with our expression for the total number of states N with energy up to E. First, we express the number of states with wave vector less than k and then convert from k to E.

The total number of states (including spin) with energy less than or equal to E is:

$$N(E) = \frac{V}{3\pi^2}k^3 \tag{5.12}$$

Using the energy relation $E = \hbar^2 k^2/(2m)$, we can write $k = \sqrt{2mE}/\hbar$. Substituting this gives:

$$N(E) = \frac{V}{3\pi^2}\left(\frac{2mE}{\hbar^2}\right)^{3/2} = \frac{V}{3\pi^2}\frac{(2m)^{3/2}}{\hbar^3}E^{3/2} \tag{5.13}$$

The density of states per unit volume is then the derivative of $N(E)/V$ with respect to energy:

$$g(E) = \frac{1}{V}\frac{dN(E)}{dE} = \frac{d}{dE}\left[\frac{1}{3\pi^2}\frac{(2m)^{3/2}}{\hbar^3}E^{3/2}\right] \tag{5.14}$$

$$g(E) = \frac{1}{2\pi^2}\left(\frac{2m}{\hbar^2}\right)^{3/2}\sqrt{E} \tag{5.15}$$

This important result shows that for a 3D free electron gas, the number of available states grows with the square root of energy.

5.4.2 The Fermi-Dirac distribution

At any temperature $T > 0$, thermal energy can excite electrons. The probability that a state with energy E is occupied by an electron is given by the **Fermi-Dirac distribution function**:

$$f(E) = \frac{1}{e^{(E-\mu)/k_BT} + 1} \tag{5.16}$$

where k_B is the Boltzmann constant and μ is the **chemical potential**. The chemical potential is the energy required to add one more electron to the system. At $T = 0$, the distribution is a step function: $f(E) = 1$ for $E < E_F$ and $f(E) = 0$ for $E > E_F$. In this limit, the chemical potential is equal to the Fermi energy, $\mu(T = 0) = E_F$.

For temperatures above absolute zero, the step function is "smeared out" over an energy range of a few k_BT around the Fermi energy. This smearing signifies that some electrons with energies just below E_F are excited to states with energies just above E_F. Since $E_F \gg k_BT$ for metals even at high temperatures, only a small fraction of the electrons are affected by temperature, which has profound consequences for properties like heat capacity and conductivity.

5.5 Consequences and applications of the model

Armed with the concepts of the Fermi energy and Fermi-Dirac statistics, we can now evaluate the model's ability to explain key physical properties of metals.

5.5.1 Electrical conductivity and Ohm's law

The model provides a microscopic basis for Ohm's Law by considering electrons accelerating under an electric field $\vec{E}$ while undergoing scattering events. The equation of motion for an electron's drift velocity $\vec{v}_d$ is given by the Drude model:

$$m\frac{d\vec{v}_d}{dt} = -e\vec{E} - \frac{m\vec{v}_d}{\tau} \tag{5.17}$$

where $-e$ is the electron charge and τ is the *relaxation time*, the average time between scattering events. In steady state ($d\vec{v}_d/dt = 0$), the drift velocity is constant:

$$\vec{v}_d = -\frac{e\tau}{m}\vec{E} \tag{5.18}$$

The electric current density $\vec{j}$ is the product of charge density (ne) and drift velocity.

$$\vec{j} = (-e)n\vec{v}_d = (-e)n\left(-\frac{e\tau}{m}\vec{E}\right) = \frac{ne^2\tau}{m}\vec{E} \tag{5.19}$$

This is precisely Ohm's Law, $\vec{j} = \sigma\vec{E}$, where the electrical conductivity σ is:

$$\sigma = \frac{ne^2\tau}{m} \tag{5.20}$$

The quantum contribution here is crucial: because of the Pauli exclusion principle, only electrons near the Fermi surface can scatter into empty states. Therefore, the relevant speed for these electrons is the Fermi velocity $v_F = \hbar k_F/m$, and the relaxation time is determined by the mean free path λ_F of these specific electrons, $\tau \approx \lambda_F/v_F$.

5.5.2 Electronic heat capacity

One of the major failures of classical physics was the "heat capacity puzzle." Classically, every free electron should contribute $\frac{3}{2}k_B$ to the heat capacity, leading to a large value $C_V = \frac{3}{2}Nk_B$. Experiments, however, showed that the electronic contribution was much smaller and proportional to temperature.

The Sommerfeld model resolves this brilliantly. When a metal is heated from $T = 0$ to a temperature T, only electrons within an energy range of approximately k_BT around the Fermi energy are excited into available states above E_F. The vast majority of electrons deep within the Fermi sea cannot be excited because the states just above them are already occupied.

The number of "thermally active" electrons is roughly $N_{\text{eff}} \approx g(E_F) \cdot k_BT$. Each of these electrons gains an average energy of about k_BT. Thus, the increase in total internal energy ΔU is:

$$\Delta U \approx N_{\text{eff}} \cdot (k_BT) \approx g(E_F)(k_BT)^2 \tag{5.21}$$

The electronic heat capacity $C_{el} = dU/dT$ is therefore proportional to the temperature. A more rigorous calculation using the Sommerfeld expansion yields:

$$C_{el} = \frac{\pi^2}{3} g(E_F) k_B^2 T = \frac{\pi^2}{2} N k_B \left(\frac{T}{T_F} \right) \tag{5.22}$$

where $T_F = E_F/k_B$ is the Fermi temperature. This linear dependence on T is a major triumph of the model and agrees well with experimental measurements at low temperatures, where it can be distinguished from the lattice heat capacity ($\propto T^3$).

5.5.3 Thermal conductivity and the Wiedemann-Franz law

In metals, heat is primarily transported by the same free electrons that conduct electricity. The thermal conductivity κ can be estimated from kinetic theory as $\kappa \approx \frac{1}{3} c_v v^2 \tau$, where c_v is the heat capacity per unit volume.

Applying quantum principles, we must use the electronic heat capacity per unit volume $c_{el} = C_{el}/V$ and the Fermi velocity v_F:

$$\kappa = \frac{1}{3} c_{el} v_F^2 \tau = \frac{1}{3} \left(\frac{\pi^2}{2} n k_B \frac{T}{T_F} \right) v_F^2 \tau \tag{5.23}$$

The Wiedemann-Franz law is an empirical observation that the ratio of thermal to electrical conductivity for metals is directly proportional to temperature. Let's test this with our model by computing the ratio κ/σ, known as the Lorenz number L:

$$L = \frac{\kappa}{\sigma T} = \frac{\frac{1}{3} \left(\frac{\pi^2}{2} n k_B^2 \frac{1}{E_F} \right) v_F^2 \tau}{\left(\frac{n e^2 \tau}{m} \right)} \tag{5.24}$$

Using $E_F = \frac{1}{2} m v_F^2$, the equation simplifies dramatically. The density n, relaxation time τ, and mass m cancel out:

$$L = \frac{\frac{\pi^2}{6} \frac{n k_B^2}{\frac{1}{2} m v_F^2} v_F^2 \tau}{\frac{n e^2 \tau}{m}} = \frac{\pi^2 k_B^2 m v_F^2 \tau}{3 m v_F^2 n e^2 \tau} = \frac{\pi^2 k_B^2}{3 e^2} \tag{5.25}$$

The model predicts that the Lorenz number $L = \kappa/(\sigma T)$ is a universal constant for all metals:

$$L = \frac{\pi^2}{3} \left(\frac{k_B}{e} \right)^2 \approx 2.44 \times 10^{-8}\, \mathrm{W \Omega K^{-2}} \tag{5.26}$$

This remarkable result, which is in excellent agreement with experimental values, is another major success of the free electron model, beautifully linking the thermal and electrical properties of metals through fundamental constants.

5.6 Limitations and failures of the free electron model

Despite its successes, the free electron model is built on a foundation of radical simplifications. As pointed out critically by Ashcroft and Mermin, these simplifications lead to several profound failures and inconsistencies that highlight the model's limitations. The primary error is ignoring the effects of the periodic potential created by the crystal lattice.

5.6.1 The classification of materials: Metals vs. insulators

The most fundamental failure of the model is its inability to explain the existence of insulators and semiconductors. According to the free electron model, any element with valence electrons should be a metal, as these electrons would form a partially filled sea of energy states capable of conducting electricity.

The model cannot answer a simple question: Why is Sodium (Na), with one valence electron, a good metal, while Diamond (C), with four valence electrons, is a superb insulator? It offers no mechanism to explain the vast differences in conductivity across materials. This failure stems directly from ignoring the electron-ion interaction, which in reality creates a structured landscape of allowed energy bands and forbidden energy gaps. The existence of an energy band gap is the defining characteristic of semiconductors and insulators, a concept entirely absent from the free electron picture.

5.6.2 Anomalies in transport properties: The Hall effect

The Hall effect provides a method for measuring the sign and density of charge carriers. In the free electron model, the Hall coefficient R_H has a simple and unambiguous prediction:

$$R_H = -\frac{1}{ne} \tag{5.27}$$

Since the electron density n and the elementary charge e are positive, the model predicts that the Hall coefficient must **always be negative** for all metals, as the charge carriers are electrons.

However, experiments show that for several metals, such as Beryllium (Be), Zinc (Zn), and Aluminum (Al), the Hall coefficient is **positive**. This suggests that the charge carriers behave as if they have a positive charge. The free electron model has no explanation for these "holes," which are a direct consequence of the band structure in real solids.

5.6.3 The mean free path paradox

While the model provides the correct functional form for conductivity, the values it requires are problematic. To match experimental conductivities, the electron mean free path λ (the average distance an electron travels between collisions) must be on the order of tens to hundreds of angstroms. This is difficult to reconcile with the picture of a dense solid, where the ions are only a few angstroms apart. Classically, one would expect an electron to scatter off nearly every ion in its path, leading to a much shorter mean free path. The model fails to explain why electrons appear to ignore the vast majority of the ions in the lattice.

This paradox is only resolved by band theory, which shows that a quantum mechanical electron wave (a Bloch wave) travels through a *perfectly periodic* potential without any scattering at all. Scattering only occurs from *deviations* from perfect periodicity, such as lattice vibrations (phonons) and impurities.

5.6.4 Cohesion and crystal structure

The free electron model treats the positive ions as a uniform "jellium." It offers no mechanism to explain why the ions, which mutually repel each other, form a stable, solid lattice. While the electron gas provides some electrostatic "glue," the model is insufficient for calculating cohesive energies accurately.

More importantly, it completely fails to explain why different metals adopt different crystal structures (e.g., BCC, FCC, HCP). If the background potential is uniform, there should be no energetic preference for one structure over another. The specific arrangement of atoms in a crystal is a direct result of the complex interplay between the electron wavefunctions and the discrete ion potentials, a phenomenon the free electron model cannot capture.

In conclusion, the failures of the free electron model are as instructive as its successes. They force us to recognize that a complete theory of solids must account for the periodic potential of the crystal lattice. This leads directly to the development of band theory, which successfully resolves these shortcomings and provides a far more powerful and accurate description of electrons in solids.

Bibliografia

[1] C. Kittel, Introduction to solid state physics, 8th ed. Hoboken, NY: Wiley (2005).

[2] Steven H. Simon, The Oxford Solid State Basics-Oxford University Press (2013).

[3] Poole Jr, Charles P. Encyclopedic dictionary of condensed matter physics. Academic Press (2004).

[4] Neil W. Ashcroft, N. David Mermin, Holt, Rinehart and Winston, Solid State Physics. Saunders College Publishing (1976).